A Large West Antarctic Ice Sheet Explains Early Neogene Sea-Level Amplitude

J. Marschalek, L. Zurli, F. Talarico, T. van de Flierdt, P. Vermeesch, A. Carter, F. Beny, V. Bout-Roumazeilles, F. Sangiorgi, S. Hemming, et al.

A Large West Antarctic Ice Sheet Explains Early Neogene Sea-Level Amplitude

J.W. Marschalek[1], L. Zurli[2], F. Talarico[2], T. van de Flierdt[1], P. Vermeesch[3], A. Carter[4], F. Beny[5], V. Bout-Roumazeilles[5], F. Sangiorgi[6], S.R. Hemming[7], L.F. Pérez[8,9], F. Colleoni[10], J. Prebble[11], T.E. van Peer[3,12], M. Perotti[2], A.E. Shevenell[13], I. Browne[13], D.K. Kulhanek[14], R. Levy[11,15], D. Harwood[16], N.B. Sullivan[17], S.R. Meyers[17], E.M. Griffith[18], C.-D. Hillenbrand[8], E. Gasson[19], M.J. Siegert[1,20], B. Keisling[7], K.J. Licht[21], G. Kuhn[22], J.E. Dodd[23], C. Boshuis[6] , L. De Santis[10], R.M. McKay[15]*

[1]Department of Earth Science and Engineering, Imperial College London, Exhibition Road, London, SW7 2AZ, UK; j.marschalek18@imperial.ac.uk

[2]Department of Physical, Earth and Environmental Sciences, University of Siena, via Laterina 8, 53100 Siena, Italy

[3]Department of Earth Sciences, University College London, UK

[4]Department of Earth and Planetary Sciences, Birkbeck, University of London, UK

[5]Laboratoire d'Océanologie et de Géosciences, UMR 8187 CNRS/Univ Lille/ULCO, 8 Cité scientifique, F-59655 Villeneuve d'Ascq, France.

[6] Department of Earth Sciences, Marine Palynology and Paleoceanography, University of Utrecht, The Netherlands

[7]Lamont-Doherty Earth Observatory of Columbia University Palisades, New York, USA

[8]British Antarctic Survey, High Cross, Madingley Road, Cambridge, UK

[9]Department of Marine Geology, C.F Møllers Allé 8, Bygning 1110, Office: 226 DK-8000 Aarhus C, Denmark.

[10]Geophysics Division, National Institute of Oceanography and Applied Geophysics – OGS, Trieste, Italy

[11]GNS Science, Lower Hutt, New Zealand.

[12]National Oceanography Centre Southampton, University of Southampton Waterfront Campus, Southampton, UK

[13]College of Marine Science, University of South Florida, St. Petersburg, FL, 33701, USA

[14]International Ocean Discovery Program, Texas A&M University, TX, USA

[15]Antarctic Research Centre, Victoria University of Wellington, Wellington, New Zealand

[16]Department of Earth and Atmospheric Sciences, University of Nebraska-Lincoln, Lincoln, NE 68588-0340, USA

[17]Department of Geoscience, University of Wisconsin-Madison, Madison, WI 53706, USA

[18]School of Earth Sciences, Ohio State University, Columbus, OH 43210, USA

[19]Centre for Geography and Environmental Sciences, University of Exeter, Penryn Campus, Cornwall, UK.

[20]Grantham Institute, Imperial College London, Exhibition Road, South Kensington, London SW7 2AZ, UK

[21]Department of Earth Sciences, Indiana University Purdue University Indianapolis, Indianapolis, USA

[22]Alfred Wegener Institute, Helmholtz Centre for Polar and Marine Research, 27568 Bremerhaven, Germany

[23]Department of Geology, Northern Illinois University, DeKalb, Illinois 60115, USA

Early to Middle Miocene sea-level oscillations of approximately 40-60 m estimated from far-field records[1,2,3] are interpreted to reflect the loss of virtually all East Antarctic ice during peak warmth[2]. This contrasts with ice-sheet model experiments suggesting most terrestrial ice in East Antarctica was retained even during the warmest intervals of the Middle Miocene[4,5]. Data and model outputs can be reconciled if a large West Antarctic Ice Sheet (WAIS) existed and expanded across most of the outer continental shelf during the Early Miocene, accounting for maximum ice-sheet volumes. Here, we provide the earliest geological evidence proving large WAIS expansions occurred during the Early Miocene (~17.72-17.40 Ma). Geochemical and petrographic data show glacimarine sediments recovered at International Ocean Discovery Program (IODP) Site U1521 in the central Ross Sea derive from West Antarctica, requiring the presence of a WAIS covering most of the Ross Sea continental shelf. Seismic, lithological and palynological data reveal the intermittent proximity of grounded ice to Site U1521. The erosion rate calculated from this sediment package greatly exceeds the long-term mean, implying rapid erosion of West Antarctica. This interval therefore captures a key step in the genesis of a marine-based WAIS and a tipping point in Antarctic ice-sheet evolution.

Introduction

Reconstructing past Antarctic ice sheet change informs predictions of the continent's contribution to future sea-level rise[6,7]. Since the 1970s, drilling efforts proximal to Antarctica have revealed the general Cenozoic evolution of Antarctic glaciation[8,9,10,11], but fundamental steps in the development of the ice sheets remain poorly constrained. One key uncertainty is the timing of West Antarctic Ice Sheet (WAIS) initiation and expansion across the outer continental shelf. Deep-sea benthic

foraminifer oxygen isotope records and Antarctic abyssal plain sedimentary sequences suggested WAIS formation occurred in the Late Miocene or early Pliocene[12,13]. However, drilling from the Antarctic margin[11,14,15] and ice-sheet modelling studies[4,5,16] have raised the possibility that WAIS expansions into areas below sea-level could have occurred during the Early Miocene or earlier, facilitated by a subaerial West Antarctic topography[17,18].

Without widespread WAIS expansions across the continental shelf in the Early Miocene, maximum ice volumes are low enough that global sea-level fluctuations of ~40-60 m estimated from far-field stratigraphic records[1] and oxygen isotope-derived ice volume estimates[2,3] require the near complete loss of the East Antarctic Ice Sheet (EAIS) during the warmest Middle Miocene periods[2]. Such an outcome is incompatible with current ice-sheet model outputs, which suggest retention of most terrestrial East Antarctic ice even during the warmest feasible Middle Miocene environmental conditions[4]. This is mainly due to hysteresis effects driven by height-mass balance feedbacks; once the ice sheet is present, parts of it can be retained in a climate warmer than that which would permit ice-sheet inception on an ice-free landscape[4,19].

Marine sediments, deposited on the continental shelf of the Ross Sea, can reveal whether the WAIS expanded across the continental shelf during the Early Miocene. However, ice proximal geological records have been hampered by poor recovery, unconformities, and/or influence from East Antarctica[9,10,11]. Seismic data suggest that significant volumes of lower Miocene glacimarine sediment exist around the West Antarctic margin[20,21,22,23]. However, seismic data require constraints from drilling to determine the age of the sediments, and to differentiate between detritus from continental-scale ice-sheet expansion and local ice caps on (paleo)topographic highs[22,23]. Consequently, WAIS grounding across the Ross Sea shelf is only clear in seismic data after the Middle Miocene Climate Transition (~14 Ma)[24,25]; it remains uncertain whether there were earlier WAIS expansions across the Ross Sea shelf.

IODP Site U1521 and Provenance Approach

IODP Expedition 374 Site U1521 (75°41.0' S, 179°40.3' W; 562 m water depth) was drilled to 650.1 metres below sea floor (mbsf) in the Pennell Basin on the outer continental shelf of the Ross Sea (Fig. 1). The site was drilled in a region that ice-sheet models indicate is one of the last locations where ice grounds during glacial maxima, making it an ideal location to assess the timing of past WAIS expansions onto the outer continental shelf[4,16,26]. The sediments from the base of the borehole up to 209.17 mbsf are split into four chronostratigraphic sequences (1-4; Fig. 2) which constitute an expanded lower Miocene section (~18 to ~16.3 Ma; see Supplementary Material for details) with 73% recovery. These sediments provide a unique window for detailed analysis of ice-sheet behaviour immediately before the onset of the Miocene Climate Optimum (MCO, ~17 Ma; Fig. 2; Extended Data Fig. 1; Extended Data Table 1).

Site U1521 sediments below 209.17 mbsf are predominantly muddy to sandy diamictites, often interbedded with thin laminae and beds of mudstone (see Supplementary Material for details)[26]. Palynological counts on 23 samples revealed sparse palynomorphs in Sequences 1 and 4A, common reworked dinoflagellate cysts in Sequence 2, and evidence for high biological productivity in Sequence 3B (Extended Data Fig. 2; Supplementary Material). These lithological and paleontological data from Sequences 1, 2, 3A and 4A indicate an ice-proximal glacimarine (and potentially subglacial) setting, while data from Sequence 3B suggest an ice-distal setting. Notably, the ~190 m thick succession of Sequence 2, containing a high proportion of reworked dinoflagellate cysts, was deposited rapidly (0.592 mm a^{-1}) within a ~317 kyr interval spanning ~17.72-17.40 Ma (Extended Data Fig. 1).

Through comparison with terrestrial rock outcrops, the sediments recovered at Site U1521 were traced back to their source regions. A differing geological history of the rocks beneath the EAIS and WAIS (Fig. 1) gives the sediment eroded by each ice sheet a distinct geochemical, petrological and mineralogical composition, allowing expansions of the EAIS and WAIS to be distinguished. To avoid bias towards, or omission of, any lithologies, we applied multiple sediment provenance

proxies[27]. Specifically, we analysed the detrital fine fraction of 37 samples for neodymium (Nd) and strontium (Sr) isotope compositions (<63 μm) and 23 samples for clay mineralogy (<2 μm). Eight samples were also processed for U-Pb dating of detrital zircons (<300 μm) and five for $^{40}Ar/^{39}Ar$ dating of detrital hornblende grains (150-300 μm). Additionally, the petrological composition of 15,740 clasts >2 mm was identified down-core (Extended Data Fig. 3).

Evidence for Early Miocene WAIS Growth

At Site U1521, detrital ε_{Nd} values are consistently more radiogenic (higher) in Sequence 2 compared to the sediments above and below (Fig. 2e), implying a contribution from a more radiogenic end member. This end member can be traced to beneath the WAIS; the ε_{Nd} values, ranging between -7.2 and -5.9, are in good agreement with measurements of Upper Quaternary diamicts from the eastern Ross Sea shelf, adjacent to West Antarctica[28]. Here, the radiogenic end member is hypothesised to be the Cenozoic alkali volcanic rocks of Marie Byrd Land, West Antarctica (Extended Data Fig. 4)[28]. Subaerial outcrops of the Marie Byrd Land volcanic province are limited, but magnetic and gravity anomalies associated with subglacial cone-shaped structures indicate the presence of numerous subglacial volcanoes (Fig. 1)[29]. We hypothesize that the Marie Byrd Land volcanic province is the more radiogenic end member in Sequence 2. Conversely, the less radiogenic (lower) ε_{Nd} values seen in Sequences 1, 3A and 4A reflect a mixture of lithologies present in the (East Antarctic) Transantarctic Mountains and fall within the range of Upper Quaternary Ross Sea tills of Transantarctic Mountain provenance (Extended Data Figs. 4, 5)[28,30]. These less radiogenic sediments also show higher and more variable magnetic susceptibility (Fig. 2)[26]. The patterns seen in the ε_{Nd} data are broadly mirrored by detrital Sr isotope compositions (Extended Data Fig. 2).

Single-grain geochronology/thermochronology and clast petrography provide insights into specific source terranes. In the Transantarctic Mountains, Precambrian rocks were affected by the pervasive Ross Orogeny (615-470 Ma), which was accompanied by intrusive felsic magmatism

(Supplementary Material)[31]. Zircon age populations from Sequences 1, 3A and 4A show a strong peak towards the earlier part of the Ross Orogeny (595 to 535 Ma) and a 6 to 21% population of Archaean and Paleoproterozoic (>1600 Ma) zircon grains (Figs. 1, 3). These features, together with a lack of grains younger than 250 Ma, resemble data from moraines in the Transantarctic Mountains[32,33,34]. Clasts in sequences 1, 3A and 4A also correlate with rocks in the Transantarctic Mountains, with lithologies including common felsic granitoids and meta-sediments alongside rarer limestones, marbles and sandstones (Extended Data Fig. 3)[31]. Although a relatively minor component, dolerite clasts are found throughout Sequences 1, 3A and 4A (Fig. 2g) and can be traced to the Jurassic Ferrar Group, which predominantly crops out in the Transantarctic Mountains (Fig. 1). Furthermore, rare *Protohaploxypinus* pollen, a distinctive component of the Permian Beacon Supergroup in the Transantarctic Mountains, are observed in Sequence 3A[35]. Overall, the sediments comprising Site U1521 Sequences 1, 3A and 4A are predominantly sourced from erosion of the Transantarctic Mountains in East Antarctica.

In contrast, Sequence 2 is characterized by the highest ε_{Nd} values and contains zircons with Cretaceous (~100 Ma) U-Pb ages (n = 16; Fig. 3a). Such ages are indicative of a West Antarctic provenance as they are presently only found beneath the modern Siple Coast ice streams, including Kamb Ice Stream and those closer to Marie Byrd Land[33,36]. The age spectra of samples from Sequence 2 share other features with data from the Siple Coast ice streams, including a broad Triassic (~240-190 Ma) age peak, few pre-Mesoproterozoic zircons (<5 % of grains) and a young (~515-505 Ma) Ross Orogeny peak (Fig. 3)[33]. Detrital hornblende $^{40}Ar/^{39}Ar$ ages from Sequence 2 further corroborate a West Antarctic provenance. Unlike zircon grains, which can survive multiple sedimentary cycles, hornblende grains are less resistant to weathering. The absence of Grenvillian (~1100-900 Ma) ages in the Sequence 2 hornblende sample (Extended Data Fig. 6) therefore suggests a West Antarctic provenance, as Grenville-age rocks are absent there[37]. The scarcity of Ferrar Group dolerite clasts, common in the Transantarctic Mountains, is also consistent with a West

Antarctic provenance (Figs. 1, 2), as is a high proportion of smectite in the clay fraction at the bottom of Sequence 2 (≤58%; Extended Data Fig. 3), with smectite percentages similar to Quaternary sediments in the eastern Ross Sea[38]. Additionally, Sequence 2 contains evidence for recycling of older marine detritus, most likely from the lower Cenozoic rift-fill strata that exist in the eastern Ross Sea region of the West Antarctic Rift System[21]. This is inferred from the dominance of reworked Eocene-Oligocene species in the diatom and spore-pollen assemblages[26], alongside the common (13-21%) reworked Eocene-Oligocene marine dinocysts, which are rare (<1.5%) in younger sediments (Extended Data Fig. 2).

Smectite abundance declines significantly up-section within Sequence 2 and is accompanied by an increase in the proportion of basalt clasts (Extended Data Fig. 7). This anticorrelation is unexpected given that smectite is a weathering product of basalt and volcanic rocks. We infer that lower in Sequence 2, basaltic bedrock was predominantly weathered to smectite and was thus largely confined to the finer grain size fractions. Over time, this more weathered regolith layer was removed, leading to erosion of progressively more pristine continental detritus containing more basalt clasts. This scenario is supported by more radiogenic ε_{Nd} values measured in the <63 μm fraction lower in Sequence 2 (Fig. 2, Extended Data Fig. 7), as Marie Byrd Land basalts are more radiogenic than other lithologies (Extended Data Fig. 5). Sequence 2 (17.72-17.40 Ma) could therefore record an advance of the WAIS over parts of West Antarctica which had not been covered by grounded ice for an extended period.

Further evidence for WAIS expansion can be found in seismic data, which can trace the sediment package deposited at Site U1521 between 17.72 and 17.40 Ma (Sequence 2) across the Ross Sea continental shelf[23]. The sediment package, which is thicker towards the eastern Ross Sea (i.e., West Antarctica), contains glacial features including widespread progradational wedges and high relief morainal banks[20,21,23]. Coupled with the lithological and palynological evidence for ice proximity at Site U1521, this shows marine-terminating ice was present. Transport of large volumes of West

177 Antarctic detritus as far west as the Pennell Basin in the central Ross Sea is evident in our
178 provenance data, which, alongside common reworked marine microfossils, proves this marine-
179 terminating ice derived from an Early Miocene WAIS which intermittently extended across most of
180 the outer continental shelf.

181 Our data therefore reveal WAIS expansions across the Ross Sea continental shelf date back to at
182 least 17.72 Ma, which is significantly earlier than previously suggested[12,13,23,24,39]. Advance of the
183 WAIS into marine-based areas (i.e., regions grounded mainly below sea level) at 17.72-17.40 Ma is
184 supported by a corresponding period of high sensitivity of the marine $\delta^{18}O$ record to obliquity
185 forcing (Fig. 2i). High obliquity sensitivity is considered a proxy for enhanced ice-sheet sensitivity to
186 ocean dynamics and thus the presence of marine-based ice[15].

187 **Birth of a Marine-Based WAIS**

188 The mean erosion rate for the WAIS catchments draining to the Ross Sea between 17.72 and 17.40
189 Ma can be estimated using the volume of the corresponding seismic package east of Site U1521[23].
190 Assuming that, at the time of deposition, the area of the Ross Sea drainage sector of the WAIS was
191 approximately the same as today (±20%), the inferred sediment volume requires a mean catchment
192 erosion of approximately 87 m in ~317 kyr (Extended Data Table 2). The mean erosion rate of
193 ~0.275 mm a^{-1} during this interval greatly exceeds the long-term mean rate of 0.012 mm a^{-1}
194 calculated for this part of the WAIS between 23 and 14 Ma[18]; even when the full uncertainty is taken
195 into account (Extended Data Table 2), it is still more than an order of magnitude higher. This
196 highlights the 17.72 to 17.40 Ma interval as one of unusually rapid erosion, with erosion rates
197 comparable to modern subpolar to temperate glacial catchments[40]. Transporting this large volume of
198 subglacially eroded debris quickly to the WAIS margin required abundant meltwater at the ice sheet
199 bed[41], as well as fast-flowing ice streams that extended into marine settings where broad deposition
200 took place. Ocean temperatures must therefore have been sufficiently cool to permit the advance of

marine-based ice, yet atmospheric conditions must have remained warm enough to provide sufficient precipitation to drive dynamic ice flow and enhanced basal erosion[4].

Since most of West Antarctica, apart from Marie Byrd Land, was thermally subsiding throughout the Miocene[18], the high erosion rate at 17.72 to 17.40 Ma is unlikely to have been driven by tectonic uplift. The eroded sediments therefore reflect ice expansion and enhanced glacial incision of the terrestrial West Antarctic hinterland, plus infilling of the Ross Sea basins. This erosive event occurred at a time when topographic reconstructions indicate a transition from a terrestrial West Antarctic topography (23 Ma) to a largely submarine West Antarctic topography (14 Ma)[18]. The timing and large volume of sediment deposited in Sequence 2 at Site U1521 suggests that the 17.72 to 17.40 Ma interval records a critical step in the transition of the WAIS from a largely terrestrial ice sheet to one that was primarily marine-based. This significant alteration to West Antarctic topography occurred just prior to major changes affecting the Antarctic cryosphere and global climate during the MCO[2,11]. Subglacial erosion may therefore have driven changes in ice-sheet evolution and behaviour as, after ~17.40 Ma, a greater submarine area in central West Antarctica would have made the mass-balance control of the WAIS more sensitive to external drivers such as sea level and oceanic forcing[5,16]. We propose that ice retreat at the onset of the MCO may be partially attributable to the crossing of this topographic tipping point and that Sequence 2 records the birth of a marine-based WAIS. This event dates to well before 14 Ma, the time slice at which topographic reconstructions first show a largely sub-marine West Antarctica[18].

Sea-Level Reconciliation

Grounded ice flowing from West Antarctica was close to Site U1521 towards the end of the Early Miocene. We therefore validate recent modelling studies suggesting that an ice sheet nucleating on a partially terrestrial West Antarctica could expand extensively into the marine realm under Early Miocene climatic and paleotopographic conditions[4,5,16]. Our data are consistent with an ice extent

similar to, or exceeding, the largest modelled Early to Middle Miocene Antarctic ice sheets (Fig. 1), containing ice volumes of approximately 80 m sea-level equivalent (SLE) depending on the topographic reconstruction used[4,5,16]. This expanded WAIS contained approximately 14-15 m SLE of ice, but also acted to buttress the EAIS resulting in significantly larger-than-present ice volumes[4,16]. These maximum ice volume constraints indicate that far-field sea-level amplitudes of ~40-60 m did not require the loss of nearly all terrestrial East Antarctic ice during subsequent warm periods during the MCO[1,2,3], consistent with modelled EAIS hysteresis effects[4]. By providing the earliest conclusive evidence for a large marine-based WAIS, our data also dispel long-held inferences that a WAIS, able to significantly impact global eustacy and climate, was not present until the Middle or Late Miocene[12,13,39].

References

1. Kominz, M. A. et al. Miocene relative sea level on the New Jersey shallow continental shelf and coastal plain derived from one-dimensional backstripping: A case for both eustasy and epeirogeny. Geosphere 12, 1437-1456 (2016).
2. Miller, K. G. et al. Cenozoic sea-level and cryospheric evolution from deep-sea geochemical and continental margin records. Science advances 6, p. eaaz1346 (2020).
3. Pekar, S. F., & DeConto, R. M. High-resolution ice-volume estimates for the early Miocene: Evidence for a dynamic ice sheet in Antarctica. Palaeogeogr., Palaeoclimatol., Palaeoecol. 231, 101-109 (2006).
4. Gasson, E., DeConto, R. M., Pollard, D. & Levy, R. H. Dynamic Antarctic ice sheet during the early to mid-Miocene. Proc. Natl. Acad. Sci. USA 113, 3459–3464 (2016).
5. Paxman, G. J., Gasson, E. G., Jamieson, S. S., Bentley, M. J., & Ferraccioli, F. Long-Term Increase in Antarctic Ice Sheet Vulnerability Driven by Bed Topography Evolution. Geophysical Research Letters 47, e2020GL090003 (2020).
6. Masson-Delmotte, V. et al. Information from paleoclimate archives. Climate change 383–464 (2013).
7. Kennicutt, M. C. et al. A roadmap for Antarctic and Southern Ocean science for the next two decades and beyond. Antarctic Science 27, 3-18 (2014).
8. Kennett, J. P. Cenozoic evolution of Antarctic glaciation, the circum-Antarctic Ocean, and their impact on global paleoceanography. Journal of Geophysical Research 82, 3843-3860 (1977).
9. Barrett, P. J. Characteristics of pebbles from Cenozoic marine glacial sediments in the Ross Sea (DSDP Sites 270–274) and the South Indian Ocean (Site 268). In Initial Reports of the Deep-Sea Drilling Project 28, 769-784 (1975).

10. Passchier, S., & Krissek, L. A. Oligocene–Miocene Antarctic continental weathering record and paleoclimatic implications, Cape Roberts drilling project, Ross Sea, Antarctica. Palaeogeogr., Palaeoclimatol., Palaeoecol. 260, 30-40 (2008).
11. Levy, R. et al. Antarctic ice sheet sensitivity to atmospheric CO2 variations in the early to mid-Miocene. Proceedings of the National Academy of Sciences 113, 3453-3458 (2016).
12. Zachos, J., Pagani, M., Sloan, L., Thomas, E., & Billups, K. Trends, rhythms, and aberrations in global climate 65 Ma to present. Science 292, 686-693 (2001).
13. Kennett, J.P., and Barker, P.F. Latest Cretaceous to Cenozoic climate and oceanographic developments in the Weddell Sea, Antarctica: an ocean-drilling perspective. Proc. Ocean Drill. Program Sci. Results 113, 937–960 (1990). doi:10.2973/odp.proc.sr.113.195.1990
14. Hauptvogel, D. W., & Passchier, S. Early–Middle Miocene (17–14 Ma) Antarctic ice dynamics reconstructed from the heavy mineral provenance in the AND-2A drill core, Ross Sea, Antarctica. Global and Planetary Change 82, 38-50 (2012).
15. Levy, R. H. et al. Antarctic ice-sheet sensitivity to obliquity forcing enhanced through ocean connections. Nature Geoscience 12, 132-137 (2019).
16. Colleoni, F. et al. Past continental shelf evolution increased Antarctic ice sheet sensitivity to climatic conditions. Scientific reports 8, 1-12 (2018).
17. Wilson, D. S. et al. Antarctic topography at the Eocene-Oligocene boundary, Palaeogeogr. Palaeoclimatol. Palaeoecol. 335-336, 24–34 (2012). doi:10.1016/j.palaeo.2011.05.028.
18. Paxman, G. J., Jamieson, S. S., Hochmuth, K., Gohl, K., Bentley, M. J., Leitchenkov, G., & Ferraccioli, F. Reconstructions of Antarctic topography since the Eocene–Oligocene boundary. Palaeogeogr., Palaeoclimatol., Palaeoecol. 535 (2019).
19. Gasson, E. G., & Keisling, B. A. The Antarctic Ice Sheet: A Paleoclimate Modelling Perspective. Oceanography 33, 90-100 (2020).
20. Anderson, J. B., & Bartek, L. R. Cenozoic glacial history of the Ross Sea revealed by intermediate resolution seismic reflection data combined with drill site information. The Antarctic Paleoenvironment: A Perspective on Global Change: Part One 56, 231-264 (1992).
21. De Santis, L., Anderson, J. B., Brancolini, G., & Zayatz, I. Seismic record of late Oligocene through Miocene glaciation on the central and eastern continental shelf of the Ross Sea. Geology and Seismic Stratigraphy of the Antarctic Margin 68, 235-260 (1995).
22. Gohl, K. et al. Seismic stratigraphic record of the Amundsen Sea Embayment shelf from pre-glacial to recent times: Evidence for a dynamic West Antarctic Ice Sheet. Marine Geology 344, 115-131 (2013).
23. Pérez, L.F. et al. Early-middle Miocene ice sheet dynamics in the Ross Sea embayment: results from integrated core-log-seismic interpretation. GSA Bulletin (2021).
24. Bart, P. J. Were West Antarctic ice sheet grounding events in the Ross Sea a consequence of East Antarctic ice sheet expansion during the middle Miocene? Earth and Planetary Science Letters 216, 93-107 (2003).
25. Chow, J. M., & Bart, P. J. West Antarctic Ice Sheet grounding events on the Ross Sea outer continental shelf during the middle Miocene. Palaeogeogr., Palaeoclimatol., Palaeoecol. 198, 169-186 (2003).

26. McKay, R., De Santis, L., Kulhanek, D. K., and the Expedition 374 Science Party. Ross Sea West Antarctic Ice Sheet History. College Station, Texas, International Ocean Discovery Program, Proceedings of the International Ocean Discovery Program (2019).
27. Licht, K. J., & Hemming, S. R. Analysis of Antarctic glacigenic sediment provenance through geochemical and petrologic applications. Quaternary Science Reviews 164, 1-24 (2017).
28. Farmer, G. L., Licht, K., Swope, R. J., & Andrews, J. Isotopic constraints on the provenance of fine-grained sediment in LGM tills from the Ross Embayment, Antarctica. Earth and Planetary Science Letters 249, 90-107 (2006).
29. van Wyck de Vries, M., Bingham, R. G., & Hein, A. S. A new volcanic province: an inventory of subglacial volcanoes in West Antarctica. Geological Society, London, Special Publications 461, SP461. 467 (2017).
30. Farmer, G. L., & Licht, K. J. Generation and fate of glacial sediments in the central Transantarctic Mountains based on radiogenic isotopes and implications for reconstructing past ice dynamics. Quaternary Science Reviews 150, 98-109 (2016).
31. Goodge, J. W. Geological and tectonic evolution of the Transantarctic Mountains, from ancient craton to recent enigma. Gondwana Research 80, 50-122 (2020).
32. Licht, K. J., & Palmer, E. F. Erosion and transport by Byrd Glacier, Antarctica during the last glacial maximum. Quaternary Science Reviews 62, 32-48 (2013).
33. Licht, K. J., Hennessy, A. J., & Welke, B. M. The U-Pb detrital zircon signature of West Antarctic ice stream tills in the Ross embayment, with implications for Last Glacial Maximum ice flow reconstructions. Antarctic Science 26, 687-697 (2014).
34. Bader, N. A., Licht, K. J., Kaplan, M. R., Kassab, C., & Winckler, G. East Antarctic ice sheet stability recorded in a high-elevation ice-cored moraine. Quaternary Science Reviews 159, 88-102 (2017).
35. Kyle, R.A. & Schopf, J.M. Permian and Triassic palynostratigraphy of the Victoria Group, Transantarctic Mountains: in Craddock, C., ed., Antarctic geoscience: Madison, University of Wisconsin Press, International Union of Geological Sciences, Series B-4, 649–659 (1982).
36. Perotti, M., Andreucci, B., Talarico, F., Zattin, M., & Langone, A. Multianalytical provenance analysis of Eastern Ross Sea LGM till sediments (Antarctica): Petrography, geochronology, and thermochronology detrital data. Geochemistry, Geophysics, Geosystems 18, 2275-2304 (2017).
37. Jordan, T. A., Riley, T. R., & Siddoway, C. S. The geological history and evolution of West Antarctica. Nature Reviews Earth & Environment 1, 1-17 (2020).
38. Balshaw-Biddle, K. M. Antarctic glacial chronology reflected in the Oligocene through Pliocene sedimentary section in the Ross Sea (Rice University, 1981).
39. Westerhold, T. et al. An astronomically dated record of Earth's climate and its predictability over the last 66 million years. Science 369, 1383-1387 (2020).
40. Koppes, M. et al. Observed latitudinal variations in erosion as a function of glacier dynamics. Nature 526, 100–103 (2015).
41. Alley, R. B., Cuffey, K. M., & Zoet, L. K. Glacial erosion: status and outlook. Annals of Glaciology 60, 1-13 (2019).

42. Cox S.C., Smith Lyttle B. and the GeoMAP team. SCAR GeoMAP dataset. GNS Science, Lower Hutt, New Zealand. Release v.201907 (2019). https://doi.org/10.21420/7SH7-6K05
43. Morlighem, M. et al. Deep glacial troughs and stabilizing ridges unveiled beneath the margins of the Antarctic ice sheet. Nat. Geosci. 13, 132–137 (2020). https://doi.org/10.1038/s41561-019-0510-8
44. Mouginot, J., Scheuchl, B. and Rignot. E. MEaSUREs Antarctic Boundaries for IPY 2007-2009 from Satellite Radar, Version 2. Boulder, Colorado USA. NASA National Snow and Ice Data Center Distributed Active Archive Center (2017). doi: https://doi.org/10.5067/AXE4121732AD.
45. Rignot, E., Jacobs, S. S., Mouginot, J. & B. Scheuchl. Ice-shelf melting around Antarctica. Science. 341, 266-270 (2013). https://doi.org/10.1126/science.1235798
46. Tinto, K.J. et al. Ross Ice Shelf response to climate driven by the tectonic imprint on seafloor bathymetry. Nat. Geosci. 12, 441–449 (2019). https://doi.org/10.1038/s41561-019-0370-2
47. Vermeesch, P. Statistical models for point-counting data. Earth and Planetary Science Letters 501, 112-118 (2018).
48. Ogg, J. Geomagnetic Polarity Time Scale. In Geologic Time Scale 2020 (eds. Gradstein, F. M. et al.) 159–192 (Elsevier, 2020).
49. Rae, J. W. et al. Atmospheric CO2 over the Past 66 Million Years from Marine Archives. Annual Review of Earth and Planetary Sciences 49, 599-631 (2021)
50. Vermeesch, P. Multi-sample comparison of detrital age distributions. Chemical Geology 341, 140-146 (2013).

Figure Legends

Figure 1. Site U1521 location and surrounding geology. The outcropping regional geology[42] around the Ross Sea is overlain on the BedMachine Antarctica V1 modern bed topography[43]. The MEaSUREs grounding line, ice sheet margin and basins are used[44,45] and the map was produced using ArcGIS software. IODP Site U1521 is located on the outer continental shelf of the central Ross Sea. Locations referenced in the text are labelled, including the ANDRILL 2A (AND-2A) and Cape Roberts Project 1 (CRP-1) drill sites. The white dashed line indicates the boundary between East and West Antarctic lithosphere[46]. Orange triangles show Cenozoic subglacial volcanic edifices detected based on morphological characteristics, gravity anomalies and magnetic anomalies[29]. The inset shows an ice-sheet model simulation using a 'cold' climate ('cold' orbit and a climate with 280 ppm atmospheric CO_2 concentrations) and an estimated Middle Miocene topography[4]. Provenance indicators from Site

U1521 Sequence 2 sediments are broadly consistent with an ice sheet similar to or exceeding the extent of this model output.

Figure 2. Selected provenance proxies from IODP Site U1521 compared to Early Miocene climate records. The light blue shaded section (Sequence 2) highlights the interval with sediments of predominantly West Antarctic provenance. The depth of Ross Sea Unconformity (RSU) 4a and 5 and seismic surface D-b are indicated in red[23]. a) Site U1521 inclination data after 20 mT demagnetisation (red points)[26] and polarity interpretation (white = reverse polarity, black = normal polarity, grey = no interpretation). b) Site U1521 lithostratigraphy[26]. c) Chronostratigraphic sequences. The circled letters between b) and c) mark the depths of the zircon U-Pb samples (Figure 3). d) Magnetic susceptibility measured on the whole core[26]. e) Neodymium isotope signature of the fine fraction. Error bars are 2 S.D. external reproducibility; for provenance interpretations, see Extended Data Figure 4 and references in Supplementary Material. f) Abundance of Eocene-Oligocene dinocysts as a percentage (black) and concentration (i.e., counts per gram sediment; grey). g) Dolerite clast abundance. Errors shown in f) and g) are 95% confidence intervals[47]. Magnetostratigraphic tie points between the polarity interpretations from shipboard data (a)[26] and geomagnetic polarity timescale (h)[48] are marked by purple dashed lines. i) Obliquity sensitivity, indicating the strength of obliquity in the $\delta^{18}O$ record relative to the theoretical strength of obliquity forcing. This has been interpreted as representing the presence of marine-based Antarctic ice[15]. j) Sea-level record based on an oxygen isotope splice[2]. Red and blue shaded intervals indicate pronounced sea-level highstands (>40 m) and lowstands (<-20 m), respectively. MCO = Miocene Climatic Optimum. k) CO_2 reconstruction with a LOESS smoothing (shaded region indicates 1 sigma error)[49]. l) Simplified lithological log from the AND-2A record, with diamictites differentiated based on a grounding-zone proximal vs distal glacimarine depositional setting[11,15].

Figure 3. Site U1521 detrital zircon U-Pb age distributions. a) Data displayed as kernel density estimates (KDEs). When present, large Ross Orogeny (~600-500 Ma), Triassic (~240-190 Ma) and Cretaceous (~100 Ma) age peaks are labelled. The age ranges of the Ross Orogeny, Grenville Orogeny and a ~2.7 Ga event recorded in Ross Sea sedimentary strata are illustrated using grey-shaded bars. The sub-bottom depth midpoints of the samples are shown in Figure 2 and listed in the methods section. b) Same data as in a), displayed as a multi-dimensional scaling (MDS) map calculated using the Kolmogorov–Smirnov statistic[50]. Stress (a measurement of the goodness of fit between the disparities and the fitted distances[50]) = 0.072. A MDS plot visualises the degree of similarity between samples, with the proximity of sample points reflecting their similarity. The axis scales are dimensionless and have no physical meaning. The colour of Site U1521 samples (A to I) corresponds their ε_{Nd} value. Previously published zircon U-Pb data from Kamb, Whillans and Bindschadler ice streams in West Antarctica, as well as Transantarctic Mountain moraines from inland and coastal regions, are shown in grey[32,33,34]. The KDEs and region of the MDS plot interpreted as having a West Antarctic provenance are shaded in light blue, consistent with the blue shading in panel a) and Figure 2. Note that although Whillans Ice Stream drains the WAIS, it is excluded from the blue shaded area due to its proximity to the Transantarctic Mountains (Figure 1), resulting in a subglacial sediment provenance signature indistinguishable from East Antarctic detritus[33].

Methods

Neodymium and Strontium Isotopes

Samples were disaggregated and wet sieved to isolate the <63 μm fraction, which was then dried at 60°C. This size fraction represents the bulk composition, as samarium and neodymium are incorporated in equal proportions into most rock-forming minerals, meaning grain-size sorting is not likely to impact results[51,52]. However, the Rb-Sr system is subject to elemental fractionation during

weathering and grain-size sorting, which can influence $^{87}Sr/^{86}Sr$ ratios (see 'Provenance Changes within Sequence 2' section in Supplementary Material). To remove authigenic Fe-Mn oxyhydroxide phases, samples were leached in a mixture of 0.05 M hydroxylamine hydrochloride, 15% acetic acid, and 0.03 M EDTA at a pH of 4[53]. A carbonate removal step was not included due to the very low carbonate content[26]. Leached sediment was dried, homogenised, and 50 mg aliquots were digested on a hotplate in concentrated HF (2 mL), $HClO_4$ (0.8 mL) and HNO_3 (1 mL) for three to five days, with a subsequent 6 M HCl step. The Nd was isolated from the sample matrix using a cation exchange resin (AG50W-X8, 200-400 μm mesh) and HCl in increasing molarity, followed by a low molarity HCl Ln-Spec resin procedure (50–100 μm mesh). The sample matrix from the cation exchange step was dried down, taken up in HNO_3, then loaded onto Eichrom Sr Spec resin to wash down the matrix and elute the Sr[54].

Neodymium isotopes were measured in the MAGIC laboratories at Imperial College London on a Nu high resolution multi-collector inductively coupled plasma mass spectrometer (HR MC-ICP-MS). To account for instrumental mass bias, isotope ratios were corrected using an exponential law and a $^{146}Nd/^{144}Nd$ ratio of 0.7219. Although negligible, interference of ^{144}Sm on ^{144}Nd was corrected for. Bracketing standards were used to correct measured $^{143}Nd/^{144}Nd$ ratios to the commonly used JNdi-1 value of 0.512115[55]. USGS BCR-2 rock standard was processed alongside all samples and yielded $^{143}Nd/^{144}Nd$ ratios consistently within error of the published ratio of 0.512638 ± 0.000015[56]. Full procedural blanks for Nd ranged from 7 to 30 pg (n = 6). $^{143}Nd/^{144}Nd$ ratios are expressed using epsilon notation (ε_{Nd}), which denotes the deviation of a measured ratio from the modern Chondritic Uniform Reservoir (0.512638)[57] in parts per 10,000.

Strontium isotopes were measured in the MAGIC laboratories at Imperial College London on a TIMS (Thermal Ionisation Mass Spectrometer). 10% of the sample was loaded in 1 μL of 6M HCl onto degassed tungsten filaments with 1 μL of $TaCl_5$ activator. The measured $^{87}Sr/^{86}Sr$ ratios were corrected for instrumental mass bias using an exponential law and an $^{88}Sr/^{86}Sr$ ratio of 8.375.

Interference of ^{87}Rb was corrected for using an $^{87}Rb/^{85}Rb$ ratio of 0.386. Analyses of the NIST 987 standard reference material were completed every four unknowns, yielding a mean of 0.710290 ± 0.000041 (2SD, n = 36). Samples were corrected to the published value of 0.710252 ± 0.000013[56]. The relatively poor reproducibility for our NIST 987 runs was due to technical issues, but is still more than sufficient for interpreting sample results, which change in the 3rd to 4th digit. Accuracy of results was confirmed using rock standard USGS BCR-2, processed with every batch of samples, which yielded $^{87}Sr/^{86}Sr$ ratios of 0.705010 ± 0.00029 (2SD, n = 18). This is well within error of the published ratio of 0.705013 ± 0.00010[56].

Detrital Zircon U-Pb Dating

The sub-bottom depth midpoints of the nine samples are: A: 220.23, B: 270.03, C: 335.72, D: 373.58, E: 410.82, F: 487.40, G: 546.55, H: 588.00 and I: 642.21 mbsf. To ensure there were enough grains for statistical analysis, the above samples were taken over 40 cm intervals. Samples were disaggregated, dried and sieved at 300 μm. Zircons from the <300 μm fraction were concentrated using standard gravity settling and magnetic separation techniques. Samples were then mounted in resin, polished and analysed using an Agilent 7900 laser ablation inductively-coupled plasma mass spectrometer (LA-ICP-MS) with a 25-35 μm pit diameter in the London Geochronology Centre at University College London. Approximately 150 grains resembling zircons were randomly selected for analysis from each sample. Plešovice zircon[58] was used as a primary standard to correct for instrumental mass bias and depth-dependent inter-element fractionation. Approximate U and Th concentrations were calculated by comparison with NIST 612 glass[59].

Data reduction of the time-resolved mass spectrometer data was performed using GLITTER 4.5[(60)]. Ages younger than 1100 Ma were calculated using the $^{206}Pb/^{238}U$ ratio whilst older grains used the $^{207}Pb/^{206}Pb$ ratio. Data were filtered to exclude non-zircons based on zirconium concentrations (>10^6 counts per second) and a -5/+15% discordance threshold was applied. This yielded at least 92 grains

per sample, giving a 95% confidence that any age populations comprising more than 7% of the sample will be measured[61]. GJ1 zircon[62] was used as a secondary standard to verify accuracy of the data. Repeat analyses using zircons with and without existing ablation pits were made to check sample reproducibility; these agreed within the uncertainties associated with random sampling. Final data were processed and visualised using the R package IsoplotR[63].

Clast Petrography

The gravel fraction (>2 mm) was characterized in continuum along the core between 648.17 and 209.17 mbsf. Clasts exposed in the cut surface of the archive half core were measured, logged and described on the basis of macroscopic features (e.g. shape, colour, texture). Logging aimed to identify the distribution and variation of the gravel-size clasts along the core length. Clast logging followed the methods previously applied to the ANDRILL and Cape Roberts Project drill records from the Ross Sea. On the basis of macroscopic features, clasts were grouped into seven main lithological groups: igneous rocks, quartz fragments, dolerites, volcanic rocks, metamorphic rocks, sedimentary rocks and sedimentary intraclasts[64,65,66,67]. Data processing involved counting the occurrence of each lithological group over 10 cm core intervals and summarizing this for each core (Extended Data Fig. 3). The total number of clasts was also summed for each metre interval (Extended Data Fig. 3). To highlight the along-core variation in dolerite and volcanic clasts - two of the most indicative lithologies for provenance constraint - the number of these clasts was divided by the total number of clasts in each core (Extended Data Fig. 3). A total of 73 pebble to cobble-sized clasts were sampled for petrographic analysis, of which the most representative of each lithological group were analysed using standard petrographic methods with polarized light microscopy.

Palynology

Sample processing was performed at Utrecht University, following standard techniques of the Laboratory of Palaeobotany and Palynology. Samples were oven-dried and weighed (~15 g dry

497 weight sediment each). One *Lycopodium clavatum* tablet with a known amount of marker spores was
498 added for quantification of palynomorph abundances[68].

499 Samples were treated with 10% HCl (Hydrochloric acid) and cold 38% HF (Hydrofluoric acid), then
500 sieved over a 10 μm mesh with occasional mild ultrasonic treatment. To avoid any potential
501 processing-related preservation bias, no oxidation or acetolysis was carried out. The processed
502 residue was transferred to microscope slides using glycerine jelly as a mounting medium, and 2
503 slides were analysed per sample at 400× magnification. Slides were examined for detailed marine
504 palynomorphs (dinoflagellate cysts, acritarchs and other aquatic palynomorphs) and, at screening-
505 level, terrestrial palynomorphs (pollen and spore) at Utrecht University. Subsequent detailed analysis
506 of terrestrial palynomorphs on a sub-set of seven samples was undertaken at GNS Science. Of the 23
507 palynological samples analysed for dinocysts, two contained <60 dinocysts (Sequence 1; 594.48
508 mbsf and Sequence 2; 567.75 mbsf) and one was almost barren (yielding only 12 *in situ* dinocysts,
509 Sequence 3A; 374.9 mbsf). The almost barren sample is excluded from all plots. The two low
510 abundance samples are included in our plots but require careful interpretation. Samples between
511 594.48 and 567.75 mbsf and below 594.48 mbsf (cores 65R, 67R, 69R and 71R) were also checked,
512 but yielded few dinocyst specimens. Those present comprised of fragments of mostly reworked
513 dinocysts.

514 Pollen and spore identification followed taxonomic compilations[69,70], augmented by key Antarctic
515 literature[71,72,73]. For pollen and spores, scanning continued until an entire cover slide was completed,
516 or a 100 count reached. Results are presented as specimens/gram, and percentage of all terrestrial
517 palynomorphs. Dinocysts were identified based on a taxonomical index[74] and informally and
518 formally described species in the literature[75,76,77,78]. Dinocyst percentages were calculated based on
519 the total *in situ* dinocysts counted, excluding reworked specimens. The percentages of other
520 palynomorph groups such as brackish and freshwater algae (*Cymatiosphaera* spp. and *Pediastrum*
521 spp.) and reworked dinocysts were calculated using the total palynomorphs counted (Fig. 2;

Extended Data Fig. 2). *In situ* dinocyst and terrestrial palynomorph absolute abundance (specimens/g dry weight) and the absolute abundance of the other palynomorph groups were calculated by counting the amount of *Lycopodium clavatum* spores encountered, following the equation of Benninghoff (1962)[79].

Protoperidinioid (P) dinocysts are mostly represented by the genera *Brigantedinium*, *Lejeunecysta*, and *Selenopemphix*. Gonyaulacoid (G) dinocysts mostly include *Batiacasphaera* spp., *Operculodinium* spp. and *Spiniferites* spp. Protoperidinioid cyst percentages (Heterotrophic % in Extended Data Fig. 2) and percentages of the most common species (*Brigantedinium* spp. *Lejeunecysta* spp., *Selenopemphix* spp. and *Selenopemphix antarctica*) were calculated to identify productivity trends and/or the presence of sea ice (see Supplementary Material). P dinocysts are likely produced by heterotrophic dinoflagellates[80] and, at present, dominate the assemblages in Antarctic sediments in areas with high nutrients and/or (year-round) sea-ice cover. At present, samples in quasi perennial sea-ice covered areas are dominated by *Selenopemphix antarctica* (~75%), with abundant *Brigantedinium* spp. and rare occurrence of other species[81,82,83]. G cysts are generally produced by phototrophic dinoflagellates. *Operculodinium* spp. is the most abundant, has species representatives among the extant cysts and has been selected to represent temperate-warm conditions. At present, it is almost exclusively found in temperate areas of the Southern Ocean north of the Subantarctic Front and never occurs in circum-Antarctic sediments south of the Polar Front[81]. In contrast, it is common to abundant in other Antarctic warm Miocene records[84,85]. Reworked dinocysts include Eocene and Oligocene taxa (mostly *Vozzhennikovia* spp., but also few *Spinidinium* spp. and *Enneadocysta diktyostila*).

Sediment Volume Estimate

The volume of sediment comprising Sequence 2 was estimated based on seismic data for the Ross Sea continental shelf[23]. The isopach maps were developed by interpolating between available seismic

546 reflection profiles[23], giving a total volume of 175,526 ± 17,553 km^3. The 10% uncertainty accounts
547 for uncertainty in seismic velocities, which vary from 1700-2700 ms^{-1} at Site U1521 based on
548 tomography and 1970-2480 ms^{-1} based on down-hole measurements. As the provenance data suggest
549 a West Antarctic sediment source for Site U1521 Sequence 2, we assume that all the sediments east
550 of 180^o and south of 73^o are derived from West Antarctica. This is the vast majority (123,627 ±
551 12,363 km^3) of the sediment across the shelf. Our sediment volume estimate is conservative, as the
552 top of Sequence 2 (surface D-b) has been truncated across much of the continental shelf by RSU4[23].
553 Significant sediment volumes are also likely to be present beyond the edge of the seismic data from
554 the continental rise. Any sediment beneath the modern Ross Ice Shelf is also unaccounted for,
555 although this component is likely to be small.

556 To translate this sediment volume into an erosion rate, the approach and uncertainty range of Paxman
557 et al. (2019)[18] was used to account for porosity and a small biogenic sediment component (Extended
558 Data Table 2). We note that using generic values in our porosity calculation is crude, with variation
559 in the porosity of these Antarctic sediments likely to be significant[86], but nevertheless sufficient for
560 our order-of-magnitude estimate of erosion. It is reasonable to assume the major ice divides have
561 remained in largely the same positions since the Early Miocene, as indicated by various modelling
562 studies using reconstructed topographies[4,5,16]. The size of the eastern Ross Sea catchment (i.e. Ross
563 Sea sector of the WAIS) was therefore assumed to be similar to the modern, with a 20% uncertainty.
564 Some sediment in these units clearly contains reworked material; there are high concentrations of
565 Eocene-Oligocene palynomorphs and diatoms. Although this means our erosion rate is not indicative
566 of pure bedrock incision, it still represents a significant change to the topography and bathymetry of
567 West Antarctica. The material removed likely exceeds our conservative estimate of ~87 m across the
568 catchment. The 317,416 year duration is based on the cyclostratigraphic analyses described in the
569 age model section, with a 20,000 year uncertainty.

570 **IODP Site U1521 Age Model**

The age model for IODP Site U1521 uses magnetostratigraphy, biostratigraphy, cyclostratigraphy, $^{87}Sr/^{86}Sr$ dating of macrofossils, and $^{40}Ar/^{39}Ar$ ages of hornblende grains to correlate rock units to the Geomagnetic Polarity Timescale (GPTS)[48]. Key events and tie points are summarized in Extended Data Table 1 and illustrated in Extended Data Figures 1 and 8. Biostratigraphic constraints include first and last appearance datums of diatoms. The maximum and minimum age range reported for these datums are derived from total and average ranges[87,88] and hybrid range models derived from Constrained Optimization (CONOP) methods[88,89]. Hybrid range model ages are used as primary constraints for our age model. This is because they best account for up section reworking of microfossil datums, which is common in glacial sedimentary environments, whilst recognising that major down section reworking is unlikely (partly because of the rarity of bioturbated intervals). They are marked by base of arrows in Extended Data Figure 1 and mentioned in the text below. Biostratigraphic datums and magnetic polarity reversals provide tie points to construct lines of correlation (LOC) with the GPTS. The age model presented here includes the interval of West Antarctic sediment provenance (Sequence 2) and is described from the base of the borehole at 650 mbsf to 75 mbsf.

Biostratigraphic constraints through the interval from 650 mbsf to near the top of Sequence 3B (at ~286.1 mbsf) are sparse as the sediments are deeper than the Opal-CT transition and diatom preservation is relatively poor. Our correlation of the four distinct magnetozones R5, N4, R4, and N3 to the GPTS is therefore primarily based on regional correlation of prominent seismic reflectors to other dated drill cores from the Ross Sea shelf, backed up by diatom biostratigraphic constraints. The section from 650 mbsf to 567.95 mbsf at Site U1521 (Sequence 1) is characterised by reversed magnetic polarity but offers no constraints which we can confidently use for correlating this reversed interval to the GPTS. However, robust age constraint for sediments at the base of Sequence 2 can be determined through regional correlation of RSU5 to other sites where chronostratigraphic data are available. RSU5 intersects Site U1521 at 567.95 mbsf (the base of Sequence 2) and is correlated

across the Glomar Challenger Basin and tied to DSDP Site 273 at 282 mbsf[23]. The LAD of *T. praefraga* is observed at 309 mbsf in DSDP Site 273, which suggests that RSU5 is younger than 17.95 Ma at that site. RSU5 cannot be directly correlated into the western Ross Sea, but a major unconformity (U2) occurs in the AND-2A drill site at 774.94 mbsf and likely corresponds with RSU5 based on chronostratigraphy[11]. Specifically, sediments that directly underlie U2 in AND-2A are characterised by a reversed magnetic polarity and are correlated to Chron C5Er (18.636 to 18.497 Ma) based on constraints that include $^{40}Ar/^{39}Ar$ dates of 18.82 ± 0.15 Ma on pumice clasts within a tuffaceous siltstone at 831.66 mbsf. The age of sediments that overlie U2 at the AND-2A drill site are constrained by the FAD of *T. praefraga* at 771.5 mbsf (<18.46 to 18.58 Ma), and a $^{40}Ar/^{39}Ar$ date of 18.04 ± 0.31 Ma on pumice clasts within a tuffaceous siltstone at 709.17 mbsf. These observations require correlation of the reversed magnetic polarity zone that characterise the sediments above U2 to Chron C5Dr.2r (18.007 to 17.676 Ma). All evidence presented above shows that between ~18.6 and ~17.8 Ma, a significant, regionally extensive, erosional event (or series of events) created surface RSU5/U2.

Sediments deposited on top of RSU5 at Site U1521 are characterised by reversed magnetic polarity. Based on the known age of RSU5 at DSDP Site 273 and U2 at AND-2A, we correlate the top of reversed magnetozone R5 in Site U1521 to Chron C5Dr.2r. This interpretation is consistent with the observation that *T. praefraga* is not present in a diatom-bearing sample at 563 mbsf, despite comprehensive searches for this species in this sample as well as diatom-bearing samples higher in Sequence 2. As *T. praefraga* is a small and compact diatom not prone to fragmentation which would likely be preserved in the observed diatom assemblages, we are confident this absence is not a result of poor preservation below the Opal-CT transition. *T. praefraga* is a common species in upper Oligocene and lower Miocene sediments recovered from several sites across the Ross Sea, including Cape Roberts Project-2/2A, DSDP Site 273, and AND-2A[11,90,91]. The total reported CONOP model based age range for the LAD of *T. praefraga* is 17.95 to 16.82 Ma and the hybrid model range is

621 17.95 to 17.36 Ma[87,88,89]. Consequently, we view the absence of *T. praefraga* as strong evidence that
622 the sediments above 563 mbsf at Site U1521 are younger than 17.95 Ma.

623 We then correlate the magnetic polarity reversal (MPR) R5/N5 between 526.8 and 524 mbsf to
624 C5Dr.1n/C5Dr.2r (17.676 Ma), the MPR N4/R4 between 517.2 and 515.1 mbsf to C5Dr.1r/C5Dr.1n
625 (17.634 Ma), and the MPR R4/N3 between 400.5 and 397.2 mbsf to C5Dn/C5Dr.1r (17.466 Ma). We
626 extend a line of correlation from this MPR to the top of Sequence 2, where it intersects with seismic
627 surface D-b[23]. The correlation presented here by interpolating through these MPRs indicates
628 sediments in Sequence 2 span the time interval from ~17.7-17.4 Ma. The occurrence of the diatom
629 taxon *Thalassiosira* sp. cf. *T. bukryi* at 450.52 mbsf supports this correlation as the range reported for
630 this taxon at ODP Site 744 is 17.7-17.4 Ma[88,92].

631 To refine the likely sedimentation rate and timespan of Sequence 2, a cyclostratigraphic analysis was
632 conducted on clast abundance data (Extended Data Fig. 3) spanning 568 to 380 mbsf. These data
633 were analysed using TimeOpt[93], which is a statistical optimization method for astronomical time
634 scale construction and astrochronologic testing, executed by the *astrochron* package in R[94] (function
635 'timeOpt'). Given a range of plausible sedimentation rates and a series of specified astronomical
636 periodicities (for precession, obliquity, and eccentricity), TimeOpt identifies the age model that
637 results in a time-series that best aligns with the predictions of Milankovitch theory. Specifically, two
638 diagnostic attributes of the astronomical hypothesis are evaluated: the hierarchy of cyclic frequencies
639 expected of Milankovitch Cycles, $r^2_{spectral}$, and the match between eccentricity cycles and the
640 precession-band envelope, $r^2_{envelope}$[93,95]. These two values (r^2_{power} and $r^2_{envelope}$) are multiplied to
641 produce an r^2_{opt} value, which provides insight into the strength of a hypothesized astronomical signal
642 at each evaluated sedimentation rate.

643 Assuming plausible average sedimentation rates between 40 cm kyr^{-1} and 65 cm kyr^{-1}, TimeOpt
644 yields an optimal sedimentation rate of 59.2 cm kyr^{-1} for Sequence 2, with an r^2_{opt} of 0.396. To assess

645 the statistical significance of the result, a Monte Carlo astrochronologic test is conducted to evaluate
646 the null hypothesis that the observed variability in clast abundance arises entirely by stochastic
647 processes, rather than astronomical forcing. The Monte Carlo simulations are generated using the
648 function "timeOptSim", which creates a large number of similar time-series of stochastic ("red")
649 noise, to assess the probability that such datasets can produce an r^2_{opt} value comparable to the one
650 generated by the clast abundance data[93,95]. This analysis yields a p-value of 0.005, indicating that the
651 null hypothesis (i.e. the data is generated from a stochastic "red noise" process; specifically an AR1
652 process) can be rejected with a high degree of confidence. Given that the astrochronologically-
653 estimated sedimentation rate is derived independently from the paleomagnetic data, their consistency
654 is remarkable and provides strong evidence in support of an estimated duration of ~317 kyrs for
655 Sequence 2 (Extended Data Fig. 1)[26].

656 While the 'floating' TimeOpt-derived astronomical time scale preserves information about elapsed
657 time, it must be separately anchored to a specific numerical age. To do so, we use the 'slideCor'
658 function in the *astrochron* package[94]; this is an automated approach to find the optimal anchoring of
659 the floating TimeOpt-derived time scale to the theoretical astronomical solution of Laskar et al.
660 (2004)[96]. Specifically, we have applied a Taner bandpass filter[97], isolating the periods between 60 ka
661 and 27 ka for both the obliquity component of the astronomical solution[96], and for the TimeOpt-
662 derived floating astrochronology. The optimal match between the astronomical solution and floating
663 astrochronology is identified using the squared Pearson correlation coefficient.

664 Independent biostratigraphic and magnetostratigraphic constraints mean we can restrict our
665 'slideCor' assessment to a feasible ~800 ka interval; our lower limit (17.950 Ma) is based on the
666 absence of *T. praefraga* and the correlations of RSU5 described above, and our upper limit is based
667 on the C5Cr/C5Dn MPR (17.154 Ma). Since the precise relationship between clast abundance and
668 astronomical forcing is not known with certainty, any time-anchor for the astronomically calibrated
669 section should be treated as having an uncertainty of at least a full obliquity cycle (~41 ka).

Application of the slideCor function identifies two plausible regions of the astronomical solution for anchoring the Sequence 2 clast abundance data. The optimal match ($r^2 = 0.8497$) results in an astronomically calibrated section ranging from 17.601 Ma to 17.918 Ma (± 0.02 Ma). This would indicate that the interval is ~140-220 kyrs older than the age range suggested by the paleomagnetic interpretation, giving a very poor match with the measured polarities. However, a slightly less optimal match ($r^2 = 0.7704$) anchors the section to span 17.398 Ma to 17.715 Ma (± 0.02 Ma), which places it within ~40 kyrs of the paleomagnetic interpretation. This agreement of geochronological frameworks derived from paleomagnetism and astrochronology, which are broadly independent, provides strong support for the age model presented here.

Uncertainties in the magnetostratigraphic age model, most notably for Subchrons C5Dr.1n and C5Dr.1r and Chron C5Dn, may account for some of the slight disagreement with the astrochronlogical approach described above. The available astronomically tuned durations of these (sub-)chrons agree within 10%[98,99]. The small discrepancies in duration of (sub-)chrons originate from the astronomical tuning approach (carbon and oxygen isotopes tuned to eccentricity, tilt and precession at Site 1090[(98)] and carbonate content to eccentricity only at Site U1336[(99)]), as well as physical and palaeomagnetic recording processes such as bioturbation and the palaeomagnetic lock-in depth[100,101]. Paleomagnetic measurement methods are discussed in detail in the cruise report[26].

We suggest 17.95-17.40 Ma as the absolute uncertainty of the timing of Sequence 2 deposition, based on the absence of *T. praefraga* (17.95 Ma) and occurrence of MPR C5Dn/C5Dr.1r (17.466 Ma) near the top of Sequence 2. However, more precise constraint on the duration of Sequence 2 deposition can be achieved based on the remarkable agreement of sedimentation rates based on the astronomical analysis of clast data and interpolation through magnetostratigraphic tie points, which suggest deposition occurred over ~317 kyrs. Combined with the close correlation between our astrochronological analyses and the timing of MPRs, we suggest a more precise interval for the deposition of Sequence 2, spanning ~17.72-17.40 ± 0.02 Ma. The ~20 kyr error represents

695 uncertainty in the phase relationship between clast abundance and obliquity forcing. This range
696 coincides closely with many independent records indicating ice-sheet growth, including a sea-level
697 lowstand recorded on the New Jersey continental margin (~17.8-17.46 Ma)[1], evidence for ice sheet
698 growth in the AND-2A drill core sediments (~17.8-17.4 Ma)[11] and a peak in obliquity sensitivity
699 (~17.8-17.5 Ma)[15] (Fig. 2).

700 The age of Sequence 3A and 3B (324.20- 209.17 mbsf), bracketed by seismic surface D-b and
701 regional unconformity RSU4a, is difficult to tightly constrain. Diatom preservation increases
702 significantly in a sample at 286.1 mbsf at the base of Sequence 4A and the FADs of *Nitzschia sp. 17*
703 *Schrader*, *Synedropsis cheethamii*, and *Denticulopsis maccollumii* suggest sediments below this
704 stratigraphic level are older than 17 Ma. The LAD of *F. maleinterpretaria* in this sample provides a
705 minimum age constraint and suggests that the sediments below 286.1 Ma must be older than 16.41
706 Ma. These constraints require that the sediments between 344.6 and 286.3 mbsf, characterised by
707 reversed polarity, correlate with either the Subchron C5Cn.2r or the base of Chron C5Cr. Correlation
708 to the base of Chron C5Cr is our favoured option as this would indicate that the interval of time
709 missing across seismic surface D-b is relatively short, whereas regional unconformity RSU4a at the
710 top of this unit records a hiatus of longer duration. The alternative interpretation is shown with a
711 dashed line in Extended Data Figure 1.

712 We constrain the slope of the LOC through Sequence 3B based on the sedimentation rate indicated
713 for the diatom-bearing Sequence 4B as the sediments are similar, although affected by diagenesis in
714 Sequence 3B. The sedimentation rate in Sequence 3A is assumed to be comparable to the Sequence 2
715 diamicts. We also acknowledge that the actual first appearance of the diatom taxa identified in the
716 sample at 286.1 mbsf may have originally been deeper, but their presence has since been obscured by
717 diagenesis. This would require that the LOC sit to the left (younger) of its current position.
718 Therefore, we include an error box (orange box in Extended Data Fig. 1) in our age model to show

719 that the LOC could occur anywhere within this area depending on the amount of time missing across
720 D-b and the sedimentation rate during deposition. We are confident that the MPR between 400.5 and
721 397.2 mbsf (N3/R3) is C5Dn/C5Dr.1r (17.466 Ma) based on constraints above and below this
722 interval outlined above and place our LOC through the reversal. This LOC requires a time gap of ~
723 180 kyrs across regional seismic surface D-b[23] that separates Sequences 2 and 3.

724 The relatively thin interval of reversed polarity within Chron C5Dn (at ca. 380 mbsf) is not identified
725 in the current version of the GPTS (Extended Data Fig. 8), but a similar short-duration reversed
726 polarity event roughly halfway through Chron C5Dn is recorded in the AND-2A
727 magnetostratigraphic record[11]. Taking the palaeomagnetic uncertainties of ice-proximal sediments
728 into account, we hypothesise that this rarely recorded reversed polarity event could be a genuine
729 feature of the geomagnetic field that has not been detected in marine sediments due to signal
730 smoothing at low sedimentation rates[102].

731 The age of sediments above RSU4a are very well constrained by diatom data, $^{87}Sr/^{86}Sr$ ages and
732 magnetostratigraphy. The LAD of *F. maleinterpretaria* indicates that the sediments above 286.1
733 mbsf must be younger than 16.41 Ma. An $^{87}Sr/^{86}Sr$ date on shell fragments at 272.65 mbsf indicates
734 the interval with reversed polarity containing the fragments correlates with Subchron C5Cn.1r
735 (16.351 to 16.261 Ma). This correlation means that the hybrid age model underestimates the
736 maximum age of the FAD of *Nitzschia grossepunctata*, which occurs at 286.1 mbsf, and suggests the
737 age indicated by the total range model age for this datum (16.23 Ma) is more likely. Together, these
738 data indicate that the base of Sequence 4A dates to less than ~16.351 Ma. We correlate the MPR
739 (R3/N2) between 209 and 205 mbsf to C5Cn.1n/C5Cn.1r (16.261 Ma). The sequence of well-dated
740 shells through Sequence 4B allows us to correlate the sediments between 209 and 106.3 mbsf that are
741 characterised by normal polarity with Subchron C5Cn.1n (16.261 to 15.994 Ma) and the MPR
742 between 106.3 and 105.5 to C5Br/C5Cn.1n (15.994 Ma). The FADs of *Denticulopsis lauta*,
743 *Actinocyclus ingens*, *Denticulopsis hyalina*, and *Denticulopsis simonsenii* at 84.99 mbsf indicate a

major hiatus at this depth spanning from ~15.83 Ma to at least 14.48 Ma. This stratigraphic horizon correlates with RSU4, a major regional unconformity[23].

Sediment Provenace Interpretations

To interpret the provenace data from IODP Site U1521, they must be placed in a regional context. In the Supplentary Material, we therefore present a short gelogical summary of the Ross Sea secotor[31,37,103-169], including a compilation of published zircon U-Pb data[33,104-128]. We also include a more detailed discussion of our hornblende $^{40}Ar/^{39}Ar$[135,153,170-174], clast petrography, clay mineralogy[157,182-187], and palynology[35,71,77,83,188-191] datasets. Additional insights into the sediment proveance of Sequences 1, 2 and 3A are also explored[23,33,38,183,192-198]. A compliation of literature neodymium and strontium isotope data (visualised in Extended Data Figures 4 and 5) is provided in Supplementary Table 1.

Additional References

51. Goldstein, S. L., & Hemming, S. R. Long-lived isotopic tracers in oceanography, paleoceanography, and ice-sheet dynamics. Treatise on geochemistry 6, 625 (2003).
52. Garçon, M., Chauvel, C., France-Lanord, C., Huyghe, P., & Lavé, J. (2013). Continental sedimentary processes decouple Nd and Hf isotopes. Geochimica et Cosmochimica Acta, 121, 177-195.
53. Gutjahr, M., Frank, M., Stirling, C. H., Klemm, V., Van de Flierdt, T., & Halliday, A. N. Reliable extraction of a deepwater trace metal isotope signal from Fe–Mn oxyhydroxide coatings of marine sediments. Chemical Geology 242, 351-370 (2007).
54. Simões Pereira, P. et al. Geochemical fingerprints of glacially eroded bedrock from West Antarctica: Detrital thermochronology, radiogenic isotope systematics and trace element geochemistry in Late Holocene glacial-marine sediments. Earth-Science Reviews 182, 204-232 (2018).
55. Tanaka, T. et al. JNdi-1: a neodymium isotopic reference in consistency with LaJolla neodymium. Chem. Geol. 168, 279–281 (2000).
56. Weis, D. et al. High-precision isotopic characterization of USGS reference materials by TIMS and MC-ICP-MS. Geochem. Geophys. Geosyst. 7, Q08006 (2006).
57. Jacobsen, S. B. & Wasserburg, G. J. Earth planet. Sci. Lett. 50, 139 (1980).
58. Sláma, J. et al. Plešovice zircon—a new natural reference material for U–Pb and Hf isotopic microanalysis. Chemical Geology 249, 1-35 (2008).

59. Pearce, N. J. et al. A compilation of new and published major and trace element data for NIST SRM 610 and NIST SRM 612 glass reference materials. Geostandards newsletter 21, 115-144 (1997).
60. Griffin, W. L. GLITTER: data reduction software for laser ablation ICP-MS. Laser Ablation ICP-MS in the Earth Sciences: Current practices and outstanding issues, 308-311 (2008).
61. Vermeesch, P. How many grains are needed for a provenance study? Earth and Planetary Science Letters 224, 441-451 (2004).
62. Jackson, S. E., Pearson, N. J., Griffin, W. L., & Belousova, E. A. The application of laser ablation-inductively coupled plasma-mass spectrometry to in situ U–Pb zircon geochronology. Chemical geology 211, 47-69 (2004).
63. Vermeesch, P. IsoplotR: A free and open toolbox for geochronology. Geoscience Frontiers 9, 1479-1493 (2018).
64. Talarico F. & Sandroni S. Petrography, Mineral Chemistry and Provenance of Basement Clasts in the CRP-1 Drillcore (Victoria Land Basin, Antarctica). Terra Antartica 5, 601-610 (1998).
65. Talarico, F., Sandroni, S., Provenance signature of the Antarctic Ice Sheets in the Ross Embayment during the Late Miocene to Early Pliocene: the ANDRILL AND-1B core record. Global and Planetary Change 69, 103–123 (2009).
66. Talarico F., Sandroni S., Fielding C.R. & Atkins C. Variability, Petrography and Provenance of Basement Clasts from CRP-2/2A Drillcore (Victoria Land Basin, Ross Sea, Antarctica). Terra Antarctica 7, 529-544 (2000).
67. Sandroni, S., and Talarico, F. M. Petrography and provenance of basement clasts and clast variability in CRP-3 drillcore (Victoria Land Basin, Antarctica), Terra Antarctica 8, 449-467 (2001).
68. Wood, G. D., Gabriel, A. M. & Lawson, J. C. In: Palynology: Principles and Applications (Eds Jansonius, J. & McGregor, D. C.) 29–50. American Association of Stratigraphic Palynologists Foundation, Dallas, TX (1996).
69. Raine, J.I., Mildenhall, D.C., Kennedy, E.M. New Zealand fossil spores and pollen: an illustrated catalogue. In: GNS Science Miscellaneous Series No. 4, 4th edition. http://data.gns.cri.nz/sporepollen/index.htm (2011).
70. Prebble, J. G. Descriptions and occurrences of pollen and spores from New Zealand Cenozoic sediments, GNS Science Internal Report 2016/09, 137 (2016).
71. Askin, R.A. Spores and pollen from the McMurdo Sound erratics, Antarctica In: Palaeobiology and Palaeoenvironments of Eocene Rocks, McMurdo Sound, East Antarctica. Antarctic Research Series v76 (Eds. Stilwel, J.D. and Feldman, R.M.), American Geophysical Union 2000 (2000).
72. Askin, R.A. and Raine, J. I. Oligocene and Early Miocene terrestrial palynology of the Cape Roberts Drillhole CRP-2/2A, Victoria Land Basin, Antarctica. Terra Antarctica 7, 493-501 (2000).
73. Truswell, E.M. Recycled Cretaceous and Tertiary pollen and spores in Antarctic marine sediments: a catalogue. Palaeontographica Abteilung B 186, 121-174 (1983).

74. Fensome, R. A. & Williams, G. L. The Lentin and Williams index of fossil dinoflagellates. American Association of Stratigraphic Palynologists Foundation Contribution Series 42 (2004).
75. Hannah, M. J., Wilson, G. J. & Wrenn, J. H. Oligocene and miocene marine palynomorphs from CRP-2/2A, Victoria Land Basin, Antarctica. Terra Antarct. 7 503–511 (2000).
76. Hannah, M. J. The palynology of ODP site 1165, Prydz Bay, East Antarctica: a record of Miocene glacial advance and retreat. Palaeogeogr. Palaeoclimatol. Palaeoecol. 231, 120–133 (2006).
77. Clowes, C. D., Hannah, M. J., Wilson, G. J. & Wrenn, J. H. Marine palynostratigraphy of the Cape Roberts Drill-holes, Victoria Land Basin, Antarctica, with descriptions of six new species of organic-walled dinoflagellate cyst. Mar. Micropaleontol. 126, 65–84 (2016).
78. Bijl P., et al. Stratigraphic calibration of Oligocene–Miocene organic-walled dinoflagellate cysts from offshore Wilkes Land, East Antarctica, and a zonation proposal. J. Micropalaeontology 37, 105–138 (2018). https://doi.org/10.5194/jm-37-105-2018
79. Benninghoff, W. S. Calculation of pollen and spores density in sediments by addition of exotic pollen in known quantities. Pollen et Spores 6, 332–333 (1962).
80. Harland, R., & Pudsey, C. J. Dinoflagellate cysts from sediment traps deployed in the Bellingshausen, Weddell and Scotia seas, Antarctica. Mar. Micropaleontol. 37, 77-99 (1999).
81. Prebble, J. G. et al. An expanded modern dinoflagellate cyst dataset for the Southwest Pacific and Southern Hemisphere with environmental associations. Mar. Micropaleontol. 101, 33–48 (2013).
82. Hartman, J. D., Bijl, P. K., & Sangiorgi, F. A review of the ecological affinities of marine organic microfossils from a Holocene record offshore of Adélie Land (East Antarctica). Journal of Micropalaeontology 37, 445-497 (2018).
83. Zonneveld, K. A. et al. Atlas of modern dinoflagellate cyst distribution based on 2405 data points. Review of Palaeobotany and Palynology 191, 1-197 (2013).
84. Warny, S. et al. Palynomorphs from a sediment core reveal a sudden remarkably warm Antarctica during the middle Miocene. Geology 37, 955–958 (2009).
85. Sangiorgi, F., et al. Southern Ocean warming and Wilkes Land ice sheet retreat during the mid-Miocene. Nature Communications 9, 1-11 (2018).
86. Niessen, F., Gebhardt, A. C., Kuhn, G., Magens, D., & Monien, D. Porosity and density of the AND-1B sediment core, McMurdo Sound region, Antarctica: Field consolidation enhanced by grounded ice. Geosphere 9, 489-509 (2013).
87. Cody, R. D., Levy, R. H., Harwood, D. M., & Sadler, P. M. Thinking outside the zone: high-resolution quantitative diatom biochronology for the Antarctic Neogene. Palaeogeog. Palaeoclimatol. Palaeoecol. 260, 92-121 (2008).
88. Florindo, F. et al. Paleomagnetism and biostratigraphy of sediments from Southern Ocean ODP Site 744 (southern Kerguelen Plateau): implications for early-to-middle Miocene climate in Antarctica. Global and Planetary Change 110, 434–454 (2013).
89. Crampton, J. S. et al. Southern Ocean phytoplankton turnover in response to stepwise Antarctic cooling over the past 15 million years. Proc. Natl Acad. Sci. USA 113, 6868–6873 (2016).

90. Scherer, R., Bohaty, S. M., & Harwood, D. M. Oligocene and lower Miocene siliceous microfossil biostratigraphy of Cape Roberts Project Core CRP-2/2A, Victoria Land Basin, Antarctica. Terra Antartica 7, 417-442. (2000).
91. Taviani, M. et al. Palaeontological characterisation and analysis of the AND-2A core, ANDRILL Southern McMurdo Sound Project, Antarctica. Terra Antartica 15, 113-146 (2008).
92. Farmer, R.K. (2011). The application of biostratigraphy and paleoecology at Southern Ocean drill sites to resolve early to middle Miocene paleoclimatic events [M.S. thesis]. University of Nebraska-Lincoln.
93. Meyers, S. R. The evaluation of eccentricity-related amplitude modulation and bundling in paleoclimate data: An inverse approach for astrochronologic testing and time scale optimization. Paleoceanography 30, 1625-1640 (2015).
94. Meyers, S.R. astrochron: An R Package for Astrochronology (2014). http://cran.rproject.org/package=astrochron
95. Meyers, S. R. Cyclostratigraphy and the problem of astrochronologic testing. Earth-Science Reviews 190, 190-223 (2019).
96. Laskar, J. et al. (2004). A long-term numerical solution for the insolation quantities of the Earth. Astronomy & Astrophysics 428, 261-285.
97. Taner, M. T. Attributes Revisited. Technical Report. Rock Solid Images, Inc. (1992).
98. Billups et al. Astronomic calibration of the late Oligocene through early Miocene geomagnetic polarity time scale, Earth and Planetary Science Letters 224, 33-44 (2004). doi:10.1016/j.epsl.2004.05.004
99. Kochhann, K.G. et al. Eccentricity pacing of eastern equatorial Pacific carbonate dissolution cycles during the Miocene Climatic Optimum. Paleoceanography 31, 1-17 (2016). doi: 10.1002/2016PA002988
100. Suganuma, Y. et al. 10Be evidence for delayed acquisition of remanent magnetization in marine sediments: Implication for a new age for the Matuyama–Brunhes boundary. Earth and Planetary Science Letters 296, 443-450 (2010). doi:10.1016/j.epsl.2010.05.031
101. Suganuma, Y. et al. Post-depositional remanent magnetization lock-in for marine sediments deduced from 10Be and paleomagnetic records through the Matuyama–Brunhes boundary. Earth and Planetary Science Letters 311, 39-52 (2011). doi: 10.1016/j.epsl.2011.08.038
102. Roberts, A.P. & Winklhofer, M. Why are geomagnetic excursions not always recorded in sediments? Constraints from post-depositional remanent magnetization lock-in modelling. Earth and Planetary Science Letters 227, 345-359 (2004). doi: 10.1016/j.epsl.2004.07.040
103. Boger, S. D. Antarctica—before and after Gondwana. Gondwana Research 19, 335-371 (2011).
104. Siddoway, C. S. Tectonics of the West Antarctic Rift System: new light on the history and dynamics of distributed intracontinental extension. In: Cooper, A., Raymond, C. and the 10th ISAES Editorial Team (Eds.) Antarctica: A Keystone in a Changing World, 91-114. The National Academic Press, USA (2008).
105. Mukasa, S. B., & Dalziel, I. W. Marie Byrd Land, West Antarctica: Evolution of Gondwana's Pacific margin constrained by zircon U-Pb geochronology and feldspar common-Pb isotopic compositions. Geological Society of America Bulletin 112, 611-627 (2000).

106. Weaver, S. D., Adams, C. J., Pankhurst, R. J., & Gibson, I. L. Granites of Edward VII Peninsula, Marie Byrd Land: anorogenic magmatism related to Antarctic-New Zealand rifting. Earth and Environmental Science Transactions of The Royal Society of Edinburgh 83, 281-290 (1992).
107. Korhonen, F. J., Saito, S., Brown, M., Siddoway, C. S., & Day, J. M. D. Multiple generations of granite in the Fosdick Mountains, Marie Byrd Land, West Antarctica: implications for polyphase intracrustal differentiation in a continental margin setting. Journal of Petrology 51, 627-670 (2010).
108. Craddock, J. et al. Precise U-Pb zircon ages and geochemistry of Jurassic granites, Ellsworth-Whitmore terrane, central Antarctica. GSA Bulletin 129, 118-136 (2017).
109. Pankhurst, R. J., Weaver, S. D., Bradshaw, J. D., Storey, B. C., & Ireland, T. R. Geochronology and geochemistry of pre-Jurassic superterranes in Marie Byrd Land, Antarctica. Journal of Geophysical Research: Solid Earth 103, 2529-2547 (1998).
110. Flowerdew, M. J. et al. Combined U-Pb geochronology and Hf isotope geochemistry of detrital zircons from early Paleozoic sedimentary rocks, Ellsworth-Whitmore Mountains block, Antarctica. Geological Society of America Bulletin 119, 275-288 (2007).
111. Elliot, D. H., & Fanning, C. M. Detrital zircons from upper Permian and lower Triassic Victoria Group sandstones, Shackleton Glacier region, Antarctica: evidence for multiple sources along the Gondwana plate margin. Gondwana Research 13, 259-274 (2008).
112. Elliot, D. H., Fanning, C. M., & Hulett, S. R. Age provinces in the Antarctic craton: Evidence from detrital zircons in Permian strata from the Beardmore Glacier region, Antarctica. Gondwana Research 28, 152-164 (2015).
113. Goodge, J. W., Williams, I. S., & Myrow, P. Provenance of Neoproterozoic and lower Paleozoic siliciclastic rocks of the central Ross orogen, Antarctica: Detrital record of rift-, passive-, and active-margin sedimentation. Geological Society of America Bulletin 116, 1253-1279 (2004).
114. Paulsen, T. S. et al. Detrital mineral ages from the Ross Supergroup, Antarctica: Implications for the Queen Maud terrane and outboard sediment provenance on the Gondwana margin. Gondwana Research 27, 377-391 (2015).
115. Paulsen, T. S. et al. Correlation and Late-Stage Deformation of Liv Group Volcanics in the Ross-Delamerian Orogen, Antarctica, from New U-Pb Ages. The Journal of Geology 126, 307-323 (2018).
116. Goodge, J. W., Fanning, C. M., Norman, M. D., & Bennett, V. C. Temporal, isotopic and spatial relations of early Paleozoic Gondwana-margin arc magmatism, central Transantarctic Mountains, Antarctica. Journal of Petrology 53, 2027-2065 (2012).
117. Paulsen, T. S. et al. Age and significance of 'outboard' high-grade metamorphics and intrusives of the Ross orogen, Antarctica. Gondwana Research 24, 349-358 (2013).
118. Rowell, A. J. et al. An active Neoproterozoic margin: evidence from the Skelton Glacier area, Transantarctic Mountains. Journal of the Geological Society 150, 677-682 (1993).
119. Encarnación, J., & Grunow, A. Changing magmatic and tectonic styles along the paleo-Pacific margin of Gondwana and the onset of early Paleozoic magmatism in Antarctica. Tectonics 15, 1325-1341 (1996).
120. Goodge, J. W., Hansen, V. L., Peacock, S. M., Smith, B. K., & Walker, N. W. Kinematic evolution of the Miller Range shear zone, central Transantarctic Mountains, Antarctica, and

implications for Neoproterozoic to early Paleozoic tectonics of the East Antarctic margin of Gondwana. Tectonics 12, 1460-1478 (1993).
121. Van Schmus, W. R., McKenna, L. W., Gonzales, D. A., Fetter, A. H., & Rowell, A. J. U-Pb geochronology of parts of the Pensacola, Thiel, and Queen Maud mountains, Antarctica. The Antarctic Region: Geological Evolution and Processes. Terra Antartica, Siena 187, 200 (1997).
122. Stump, E. The Ross Orogen of the transantarctic mountains. Cambridge University Press (1995).
123. Martin, A. P., Price, R. C., Cooper, A. F., & McCammon, C. A. Petrogenesis of the rifted southern Victoria Land lithospheric mantle, Antarctica, inferred from petrography, geochemistry, thermobarometry and oxybarometry of peridotite and pyroxenite xenoliths from the Mount Morning eruptive centre. Journal of Petrology 56, 193-226 (2015).
124. Goodge, J. W., Myrow, P., Williams, I. S., & Bowring, S. A. Age and provenance of the Beardmore Group, Antarctica: constraints on Rodinia supercontinent breakup. The Journal of geology 110, 393-406 (2002).
125. Stump, E., Gehrels, G., Talarico, F. M., & Carosi, R. Constraints from detrital zircon geochronology on the early deformation of the Ross orogen, Transantarctic Mountains, Antarctica. In Antarctica: A Keystone in a Changing World – Online Proceedings of the 10th ISAES, edited by A.K. Cooper and C.R. Raymond et al., USGS Open-File Report 2007-1047, Extended Abstract 166 (2007).
126. Cooper, A. F., Maas, R., Scott, J. M., & Barber, A. J. Dating of volcanism and sedimentation in the Skelton Group, Transantarctic Mountains: implications for the Rodinia-Gondwana transition in southern Victoria Land, Antarctica. GSA Bulletin 123, 681-702 (2011).
127. Goodge, J. W., Fanning, C. M., & Bennett, V. C. U–Pb evidence of ~1.7 Ga crustal tectonism during the Nimrod Orogeny in the Transantarctic Mountains, Antarctica: implications for Proterozoic plate reconstructions. Precambrian Research 112, 261-288 (2001).
128. Goodge, J. W., & Fanning, C. M. Mesoarchean and Paleoproterozoic history of the Nimrod Complex, central Transantarctic Mountains, Antarctica: stratigraphic revisions and relation to the Mawson Continent in East Gondwana. Precambrian Research 285, 242-271 (2016).
129. Veevers, J. J., & Saeed, A. Age and composition of Antarctic bedrock reflected by detrital zircons, erratics, and recycled microfossils in the Prydz Bay–Wilkes Land–Ross Sea–Marie Byrd Land sector (70–240 E). Gondwana Research 20, 710-738 (2011).
130. Goodge, J. W., & Fanning, C. M. 2.5 by of punctuated Earth history as recorded in a single rock. Geology 27, 1007-1010 (1999).
131. Grindley, G. W., McGregor, V. R., & Walcott, R. I. Outline of the geology of the Nimrod-Beardmore-Axel Heiberg glaciers region, Ross Dependency. Antarctic Geology, 206-219 (1964).
132. Laird, M. G. The late Proterozoic-middle Palaeozoic rocks of Antarctica. In R. J. Tingey (Ed.) The Geology of Antarctica (pp. 74-119). Oxford University Press, Oxford (1991).
133. Goodge, J. W., & Finn, C. A. Glimpses of East Antarctica: Aeromagnetic and satellite magnetic view from the central Transantarctic Mountains of East Antarctica. Journal of Geophysical Research: Solid Earth 115 (2010).

134. Goodge, J. W., & Fanning, C. M. Composition and age of the East Antarctic Shield in eastern Wilkes Land determined by proxy from Oligocene-Pleistocene glaciomarine sediment and Beacon Supergroup sandstones, Antarctica. GSA Bulletin 122, 1135-1159 (2010).
135. Gunn, B. M., & Warren, G. Geology of Victoria Land between the Mawson and Mulock Glaciers, Antarctica. New Zea. Geol. Bull. 71, 157 (1962).
136. Encarnación, J., Rowell, A.J., Grunow, A.M. A U-Pb age for the Cambrian Taylor Formation, Antarctica: Implications for the Cambrian time scale. Journal of Geology 107, 497–504 (1999).
137. Wareham, C. D., Stump, E., Storey, B. C., Millar, I. L., & Riley, T. R. Petrogenesis of the Cambrian Liv Group, a bimodal volcanic rock suite from the Ross orogen, Transantarctic Mountains. Geological Society of America Bulletin 113, 360-372 (2001).
138. Elliot, D. H., Larsen, D., Fanning, C. M., Fleming, T. H., & Vervoort, J. D. The Lower Jurassic Hanson Formation of the Transantarctic Mountains: implications for the Antarctic sector of the Gondwana plate margin. Geological Magazine 154, 777-803 (2016).
139. Elliot, D.H., Fanning, C.M., Isbell, J.L., Hulett, S.R.W. The Permo-Triassic Gondwana sequence, central Transantarctic Mountains, Antarctica: Zircon geochronology, provenance, and basin evolution. Geosphere 13, 155–178 (2017). https://doi.org/10.1130/GES01345.1.
140. Elsner, M., Schöner, R., Gerdes, A., & Gaupp, R. (2013). Reconstruction of the early Mesozoic plate margin of Gondwana by U–Pb ages of detrital zircons from northern Victoria Land, Antarctica. Geological Society, London, Special Publications, 383(1), 211-232.
141. Paulsen, T., Deering, C., Sliwinski, J., Bachmann, O., Guillong, M. New detrital zircon age and trace element evidence for 1450 Ma igneous zircon sources in East Antarctica. Precambrian Res. 300, 53–58 (2017). http://dx.doi.org/10.1016/j.precamres.2017.07.011
142. Zurli, L. et al. Detrital zircons from Late Paleozoic Ice Age sequences in Victoria Land (Antarctica): New constraints on the glaciation of southern Gondwana. GSA Bulletin (2021) https://doi.org/10.1130/B35905.1
143. Welke, B. et al. Applications of detrital geochronology and thermochronology from glacial deposits to the Paleozoic and Mesozoic thermal history of the Ross Embayment, Antarctica. Geochemistry, Geophysics, Geosystems 17, 2762-2780 (2016).
144. Vogel, M. B., Ireland, T. R., & Weaver, S. D. The multistage history of the Queen Maud Batholith, La Gorce Mountains, central Transantarctic Mountains. In Antarctica at the close of a millennium: proceedings of the 8th International Symposium on Antarctic Earth Sciences, Wellington 1999 (2002).
145. Gootee, B., & Stump, E. Depositional environments of the Byrd Group, Byrd Glacier area: a Cambrian record of sedimentation, tectonism, and magmatism. In: Fütterer D.K., Damaske D., Kleinschmidt G., Miller H. &Tessensohn F. (Eds.) Antarctica. Springer, Berlin, Heidelberg (2006).
146. Barrett, P. J. The Devonian to Jurassic Beacon Supergroup of the Transantarctic Mountains and correlatives in other parts of Antarctica. In: The geology of Antarctica, 120-152 (1991).
147. Ferraccioli, F., Armadillo, E., Jordan, T., Bozzo, E., & Corr, H. Aeromagnetic exploration over the East Antarctic Ice Sheet: a new view of the Wilkes Subglacial Basin. Tectonophysics 478, 62-77 (2009).

148. Paxman, G. J. et al. Geology and Geomorphology of the Pensacola-Pole Basin, East Antarctica. Geochemistry, Geophysics, Geosystems 20, 2786-2807 (2019).
149. Elliot, D. H. The Hanson Formation: a new stratigraphical unit in the Transantarctic Mountains, Antarctica. Antarctic Science 8, 389-394 (1996).
150. Elliot, D. H., & Fleming, T. H. Occurrence and dispersal of magmas in the Jurassic Ferrar large igneous province, Antarctica. Gondwana Research 7, 223-237 (2004).
151. Burgess, S. D., Bowring, S. A., Fleming, T. H., & Elliot, D. H. High-precision geochronology links the Ferrar large igneous province with early-Jurassic ocean anoxia and biotic crisis. Earth and Planetary Science Letters 415, 90-99 (2015).
152. Encarnación, J., Fleming, T. H., Elliot, D. H., & Eales, H. V. Synchronous emplacement of Ferrar and Karoo dolerites and the early breakup of Gondwana. Geology 24, 535-538 (1996).
153. Cook, C. P. et al. Glacial erosion of East Antarctica in the Pliocene: A comparative study of multiple marine sediment provenance tracers. Chemical Geology 466, 199-218 (2017).
154. Adams, C. J. Geochronological studies of the Swanson Formation of Marie Byrd Land, West Antarctica, and correlation with northern Victoria Land, East Antarctica, and South Island, New Zealand. New Zealand Journal of Geology and Geophysics 29, 345-358 (1986).
155. Yakymchuk, C. et al. Anatectic reworking and differentiation of continental crust along the active margin of Gondwana: a zircon Hf–O perspective from West Antarctica. Geological Society, London, Special Publication 383 (2013). https://doi.org/10 .1144/SP383.7
156. Yakymchuk, C. et al. Paleozoic evolution of western Marie Byrd Land, Antarctica. GSA Bull. 127, 1464–1484 (2015).
157. Simões Pereira, P. et al. The geochemical and mineralogical fingerprint of West Antarctica's weak underbelly: Pine Island and Thwaites glaciers. Chemical Geology, 119649 (2020).
158. Adams, C. J. Geochronology of granite terranes in the Ford Ranges, Marie Byrd Land, West Antarctica. New Zealand journal of geology and geophysics 30, 51-72 (1987).
159. LeMasurier, W. E. et al. (1990). Volcanoes of the Antarctic Plate and Southern Ocean (Vol. 48). Washington, D.C., American Geophysical Union.
160. Licht, K. J. et al. Evidence for extending anomalous Miocene volcanism at the edge of the East Antarctic craton. Geophysical Research Letters 45, 3009-3016 (2018).
161. Brodie, J. W. A shallow shelf around Franklin Island in the Ross Sea, Antarctica. New Zealand Journal of Geology and Geophysics 2, 108-119 (1959).
162. Lawver, L., Lee, J., Kim, Y., & Davey, F. Flat-topped mounds in western Ross Sea: Carbonate mounds or subglacial volcanic features? Geosphere 8, 645-653 (2012).
163. Di Vincenzo, G., Bracciali, L., Del Carlo, P., Panter, K., & Rocchi, S. 40Ar–39Ar dating of volcanogenic products from the AND-2A core (ANDRILL Southern McMurdo Sound Project, Antarctica): correlations with the Erebus Volcanic Province and implications for the age model of the core. Bulletin of Volcanology 72, 487-505 (2010).
164. Panter, K. S. et al. Melt origin across a rifted continental margin: a case for subduction-related metasomatic agents in the lithospheric source of alkaline basalt, NW Ross Sea, Antarctica. Journal of Petrology 59, 517-558 (2018).

165. McIntosh, W. C. 40Ar/39Ar geochronology of tephra and volcanic clasts in CRP-2A, Victoria Land Basin, Antarctica. Terra Antartica 7, 621-630 (2000).
166. LeMasurier, W. E., & Rocchi, S. Terrestrial record of post-Eocene climate history in Marie Byrd Land, West Antarctica. Geografiska Annaler: Series A, Physical Geography 87, 51-66 (2005).
167. Rocchi, S., LeMasurier, W. E., & Di Vincenzo, G. (2006). Oligocene to Holocene erosion and glacial history in Marie Byrd Land, West Antarctica, inferred from exhumation of the Dorrel Rock intrusive complex and from volcano morphologies. GSA Bull. 118, 991-1005.
168. LeMasurier, W. Shield volcanoes of Marie Byrd Land, West Antarctic rift: oceanic island similarities, continental signature, and tectonic controls. Bulletin of Volcanology 75, 726 (2013).
169. Behrendt, J. C. et al. Geophysical studies of the West Antarctic rift system. Tectonics 10, 1257-1273 (1991).
170. McDougall, I. & Harrison, T. M. GEOCHRONOLOGY and THERMOCHRONOLOGY by the 40Ar/39Ar METHOD. Oxford University Press, Oxford (1999).
171. Cherniak, D. J., & Watson, E. B. Pb diffusion in zircon. Chemical Geology 172, 5-24 (2001).
172. Morrison A.D. & Reay A. Geochemistry of Ferrar Dolerite sills and dikes at Terra Cotta Mountain, south Victoria Land, Antarctica. Antarctic Science 7, 73-85 (1995).
173. Cox, S.C., Turnbull, I.M., Isaac, M.J., Townsend, D.B. & Smith Lyttle, B. Geology of southern Victoria Land, Antarctica. Institute of Geological & Nuclear Sciences geological map 22, scale 1:250 000, 1 sheet (2012).
174. Ford, A. B. Stratigraphy of the layered gabbroic Dufek intrusion, Antarctica. U.S. Geol. Surv. Bull., vol. 1405-D (1976).
175. Borg, S. G., Depaolo, D. J., & Smith, B. M. Isotopic structure and tectonics of the central Transantarctic Mountains. Journal of Geophysical Research: Solid Earth 95, 6647-6667 (1990).
176. Cox, S.C., Parkinson, D.L., Allibone, A.H. & Cooper, A.F. Isotopic character of Cambro-Ordovician plutonism, southern Victoria Land, Antarctica. New Zealand Journal of Geology and Geophysics 43, 501-520 (2000). DOI: 10.1080/00288306.2000.9514906.
177. Gunner, J. ISOTOPIC and GEOCHEMICAL STUDIES of the PRE-DEVONAIN BASEMENT COMPLEX, BEARDMORE GLACIER REGION, ANTARCTICA. Ohio State University, Columbus, Institute of Polar Studies Report No. 41 (1976).
178. Roy, M., van de Flierdt, T., Hemming, S. R., & Goldstein, S. L. 40Ar/39Ar ages of hornblende grains and bulk Sm/Nd isotopes of circum-Antarctic glacio-marine sediments: Implications for sediment provenance in the Southern Ocean. Chemical Geology 244, 507-519 (2007).
179. Behrendt, J. C. The aeromagnetic method as a tool to identify Cenozoic magmatism in the West Antarctic Rift System beneath the West Antarctic Ice Sheet—A review; Thiel subglacial volcano as possible source of the ash layer in the WAISCORE. Tectonophysics 585, 124-136 (2013).
180. Lough, A. C. et al. Seismic detection of an active subglacial magmatic complex in Marie Byrd Land, Antarctica. Nature Geoscience 6, 1031-1035 (2013).

181. Schroeder, D. M., Blankenship, D. D., Young, D. A., & Quartini, E. Evidence for elevated and spatially variable geothermal flux beneath the West Antarctic Ice Sheet. Proceedings of the National Academy of Sciences 111, 9070-9072 (2014).
182. Ehrmann, W. U., Melles, M., Kuhn, G., & Grobe, H. Significance of clay mineral assemblages in the Antarctic Ocean. Marine Geology 107, 249-273 (1992).
183. Fagel N. Clay minerals, deep circulation and climate. Proxies Late Cenozoic Paleoceanogr. 1, 139-184 (2007).
184. Kristoffersen, Y., Strand, K., Vorren, T., Harwood, D. and Webb, P. Pilot shallow drilling on the continental shelf, Dronning Maud Land, Antarctica. J. Antarct. Sci. 4, 463–470 (2000).
185. Ehrmann, W. et al. Provenance changes between recent and glacial-time sediments in the Amundsen Sea embayment, West Antarctica: clay mineral assemblage evidence. Antarctic Science 23, 471-486 (2011).
186. Hillenbrand, C. D., Grobe, H., Diekmann, B., Kuhn, G., & Fütterer, D. K. Distribution of clay minerals and proxies for productivity in surface sediments of the Bellingshausen and Amundsen seas (West Antarctica)–Relation to modern environmental conditions. Marine Geology 193, 253-271 (2003).
187. Klages, J. P. et al. Temperate rainforests near the South Pole during peak Cretaceous warmth. Nature 580, 81-86 (2020).
188. Zonneveld, K.A.F., Bockelmann, F. & Holzwarth, U. Selective preservation of organic-walled dinoflagellate cysts as a tool to quantify past net primary production and bottom water oxygen concentrations. Marine Geology 237, 109–126 (2007).
189. Prebble, J. G., Hannah, M. J., & Barrett, P. J. (2006). Changing Oligocene climate recorded by palynomorphs from two glacio-eustatic sedimentary cycles, Cape Roberts Project, Victoria Land Basin, Antarctica. Palaeogeogr., Palaeoclimatol., Palaeoecol. 231, 58-70.
190. Kulhanek, D.K. et al. Revised chronostratigraphy of DSDP Site 270 and late Oligocene to early Miocene paleoecology of the Ross Sea sector of Antarctica. Global and Planetary Change 178, 46-64 (2019).
191. Feakins, S., Warny, S. & Lee, JE. Hydrologic cycling over Antarctica during the middle Miocene warming. Nature Geosci. 5, 557–560 (2012). https://doi.org/10.1038/ngeo1498
192. De Santis, L., Prato, S., Brancolini, G., Lovo, M., & Torelli, L. The Eastern Ross Sea continental shelf during the Cenozoic: implications for the West Antarctic ice sheet development. Global and Planetary Change 23, 173-196 (1999).
193. Ford, A. B., & Barrett, P. J. Basement rocks of the south-central Ross Sea, Site 270, DSDP Leg 28. Initial Reports of the Deep Sea Drilling Project 28, 861-868 (1975).
194. Goldich, S. S., Treves, S. B., Suhr, N. H., & Stuckless, J. S. Geochemistry of the Cenozoic volcanic rocks of Ross Island and vicinity, Antarctica. The Journal of Geology 83, 415-435 (1975).
195. Tulaczyk, S., Kamb, B., Scherer, R. P., & Engelhardt, H. F. Sedimentary processes at the base of a West Antarctic ice stream; constraints from textural and compositional properties of subglacial debris. Journal of Sedimentary Research 68, 487-496 (1998).
196. Rosenqvist, I. T. Origin and mineralogy glacial and interglacial clays of southern Norway. Clays and Clay Minerals 23, 153-159 (1975).

197. Blum, J. D., & Erel, Y. Rb/ Sr isotope systematics of a granitic soil chronosequence: The importance of biotite weathering. Geochimica et Cosmochimica Acta 61, 3193-3204 (1997).
198. Eisenhauer, A. et al. Grain size separation and sediment mixing in Arctic Ocean sediments: evidence from the strontium isotope systematic. Chemical Geology 158, 173-188 (1999).

Data availability All data from this study can be found in the British Geological Survey National Geoscience Data Centre. (*6 DOIs for Nd and Sr isotope, Zircon U-Pb, Clast, Clay Mineralogy, Hornblende $^{40}Ar/^{39}Ar$ and Palynological data are currently being produced*).

Permit Antarctic Conservation Act Permit Number: ACA 2018-027 (permit holder: Bradford Clement, JRSO, IODP, TAMU, College Station, TX 77845)

Acknowledgements

This research used data and samples provided by the International Ocean Discovery Program (IODP), which is sponsored by the US National Science Foundation (NSF) and participating countries under the management of Joint Oceanographic Institutions. J.W.M. was supported by a NERC DTP studentship. Neodymium and Sr isotope analysis and U-Pb dating of detrital zircons was funded through NERC UK IODP grant NE/R018219/1. Clast counts performed by L.Z., F.T. and M.P. and the participation of L.D. and F.C. was funded by the Italian National Antarctic Research Program (PNRA - Programma Nazionale Ricerche in Antartide) - grant numbers PNRA18-00233, PNRA16-00016 and PNRA18-00002. R.M.M. was supported by Royal Society Te Apārangi Marsden Fund (18-VUW-089). L.F.P. has been funded by the European Union's Horizon 2020 research and innovation programme under the Marie Sklodowska-Curie grant agreement No. 792773 WAMSISE. D.K.K. was supported by the IODP JOIDES Resolution Science Operator and National Science Foundation (grant 1326927). Southern Transantarctic Mountain rock samples for Nd and Sr isotope analysis were provided by the Polar Rock Repository with support from the National Science Foundation, under Cooperative Agreement OPP-1643713. We thank B. Coles, K. Kreissig and P. Simões Pereira for technical support. We also thank the numerous scientists who collected invaluable

site survey data and developed the proposals and hypotheses that ultimately led to IODP Expedition 374.

Author Contributions

J.W.M., T.v.d.F, R.M.M., L.D.S. and A.E.S. designed the research in collaboration with the entire IODP Expedition 374 science party. J.W.M. conducted the Nd and Sr isotope analyses. L.Z., F.T. and M.P. performed the clast counts. J.W.M., P.V. and A.C. produced the zircon U-Pb data. F.B. and V.B.R. collected the clay mineralogy data. F.S., J.P. and C.B. performed the palynological counts and interpretations. S.R.H. provided the hornblende $^{40}Ar/^{39}Ar$ data. K.J.L. provided guidance on geochronology interpretations. L.F.P., F.C. and L.D.S. calculated the sediment volume estimate. R.L, R.M.M., T.E.v.P., D.H., D.K.K. and E.M.G. improved the shipboard age model. N.B.S and S.R.M. conducted the astrochronological analyses. D.K.K. provided the XRF data. E.G. and B.K. helped integrate sediment provenance data with numerical modelling.////// I.B., G.K., and J.E.D. advised on specific technical aspects of the manuscript. J.W.M. created the figures and wrote the text with assistance from all authors and particular guidance from T.v.d.F, C.D.H, E.G., and M.J.S.. All Expedition 374 scientists contributed to the collection of shipboard datasets and the interpretations of the data.

Consortia

IODP Expedition 374

Jeanine Ash, François Beny, Imogen M. Browne, Giuseppe Cortese, Laura De Santis, Justin P. Dodd, Oliver M. Esper, Jenny A. Gales, David M. Harwood, Saki Ishino, Benjamin A. Keisling, Sookwan Kim, Sunghan Kim, Denise K. Kulhanek, Jan Sverre Laberg, R. Mark Leckie, Robert M. McKay, Juliane Müller, Molly O. Patterson, Brian W. Romans, Oscar E. Romero, Francesca Sangiorgi, Osamu Seki, Amelia E. Shevenell, Shiv M. Singh, Isabela M. Cordeiro de Sousa, Saiko T. Sugisaki, Tina van de Flierdt, Tim E. van Peer, Whenshen Xiao and Zhifang Xiong.

Competing Interests The authors declare no competing interests.

Correspondence and requests for materials should be addressed to James W. Marschalek.

Extended Data Figure and Table Legends

Extended Data Figure 1. Age model constraints below 75 mbsf at Site U1521. From left to right are: depth (metres below sea floor), core number, core recovery (black = recovered), inclination prior to and after 10 and 20 mT demagnetisation (black, blue and red points, successively), and corresponding polarity interpretations (black = normal, white = reversed, grey = no interpretation). Note that the polarity interpretations have been simplified compared to those in the cruise report[26], with small uncertainties related to core gaps removed. Note Site U1521 is in the Southern Hemisphere. The geomagnetic polarity timescale[48] is shown across the top of the plot. The orange shaded regions indicate uncertainties in our age model and the dashed line marks an alternative line of correlation for Sequence 3. The blue line indicates the age model for Sequence 2 based on our astrochronological analyses, with the light blue shading indicating the ~20 kyr uncertainty associated with the phase relationship between clast abundances and obliquity. This astrochronological anchoring agrees closely with linear interpolations between magnetostratigraphic tie points (black line).

Extended Data Figure 2. Selected palynological counts compared to strontium and neodymium isotope data. Palynological data are reported as percentages (crosses) and counts/gram (circles). The blue shaded area represents Sequence 2, which is interpreted as consisting of sediments with a West Antarctic provenance. Error bars indicate a 95% confidence interval[47].

Extended Data Figure 3. Down-core clast and clay mineral distribution. The blue shaded area highlights Sequence 2, which is interpreted to consist of sediments with a West Antarctic provenance. a) Core lithology (see Figure 2 for key). b) Chronostratigraphic sequences. c) Clast

abundance. d) Percentages of different clast lithologies. e) Ratio between dolerite and total number of clasts (red) and volcanic rocks and total number of clasts (green), with 95% confidence interval shown as pale shading[47]. f) Clay mineral abundances.

Extended Data Figure 4. Map of approximate ε_{Nd} values in rocks and offshore sediments from around the Ross Sea embayment. Epsilon Nd values are overlain on MODIS imagery[209] and the BedMachine Antarctica V1 modern bed topography[43], with the MEaSUREs grounding line and ice sheet margin shown[44,45]. The approximate boundary between West and East Antarctic lithosphere is shown using a white dashed line[46]. Modern/late Holocene and terrestrial till samples are represented by circles with the same colour bar[28,30,54]. Although ice flow patterns have changed since their deposition, Last Glacial Maximum tills in offshore sediments are also plotted as squares to improve spatial coverage[28]. Individual samples and references are reported in Supplementary Table 1. The bedrock map was produced by Kriging between sample locations within a group, then masking to the outcrop area. Beacon and Ferrar Group (Fig. 1) rocks are often not differentiated in geological mapping, but are roughly equal volumetrically[135], with the uppermost Beacon Supergroup formations having a Ferrar-like isotopic signature[138]. We hence assume a 60% Ferrar, 40% Beacon mixture is representative.

Extended Data Figure 5. Kernel density estimate plots for literature measurements of rock ε_{Nd} compared to measurements on fine-grained Miocene detritus from Site U1521. For references and a list of all the data, see Supplementary Table 1. The height of the curve indicates the density of measurements and n the total number of samples analysed. Colour scheme is identical to Figure 1, with sediments in grey.

Extended Data Figure 6. Kernel density estimates for hornblende $^{40}Ar/^{39}Ar$ ages compared to zircon U-Pb ages younger than 1500 Ma. The two dating methods are show in red and blue, respectively. Bold letters correspond with those in Figure 3. The positions of major peaks and

number of grains analysed are labelled in the corresponding colours. Stratigraphic position is shown in Figure 2.

Extended Data Figure 7. Close up of the Site U1521 interval with a West Antarctic provenance. The stratigraphic log (a) is displayed alongside the percentage of reworked dinocysts (b), basalt clast fraction (c), relative abundance of smectite (d), Nd isotope data (e) and Fe/Ti ratios determined by X-ray fluorescence scanning (f).

Extended Data Figure 8. Correlation of Site U1521 magnetostratigraphic tie points. Shown are correlations between the AND-2A record[11], Site U1521[26] and the GPTS[48].

Extended Data Table 1. Age tie points for Site U1521 below 75 mbsf. FAD: First Appearance Datum, LAD: Last Appearance Datum. Depth errors for the biostratigraphic datums reflect the position of the first downhole sample in which the reported species was not observed. We cannot exclude the possibility that the true first observation occurs between this sample and that reported as the FAD. Opal-CT indicates that the lowermost occurrence is uncertain due to poor preservation below the Opal-CT transition (~286.1 mbsf). Age errors for the biostratigraphic events are given as the maximum and minimum reported ages based on hybrid range models[88,89]. Magnetic Polarity Reversals (MPR) depths are given as midpoints between samples with differing polarities, with the depth error indicating the distance to these samples.

Extended Data Table 2. Values used in the erosion rate calculation.

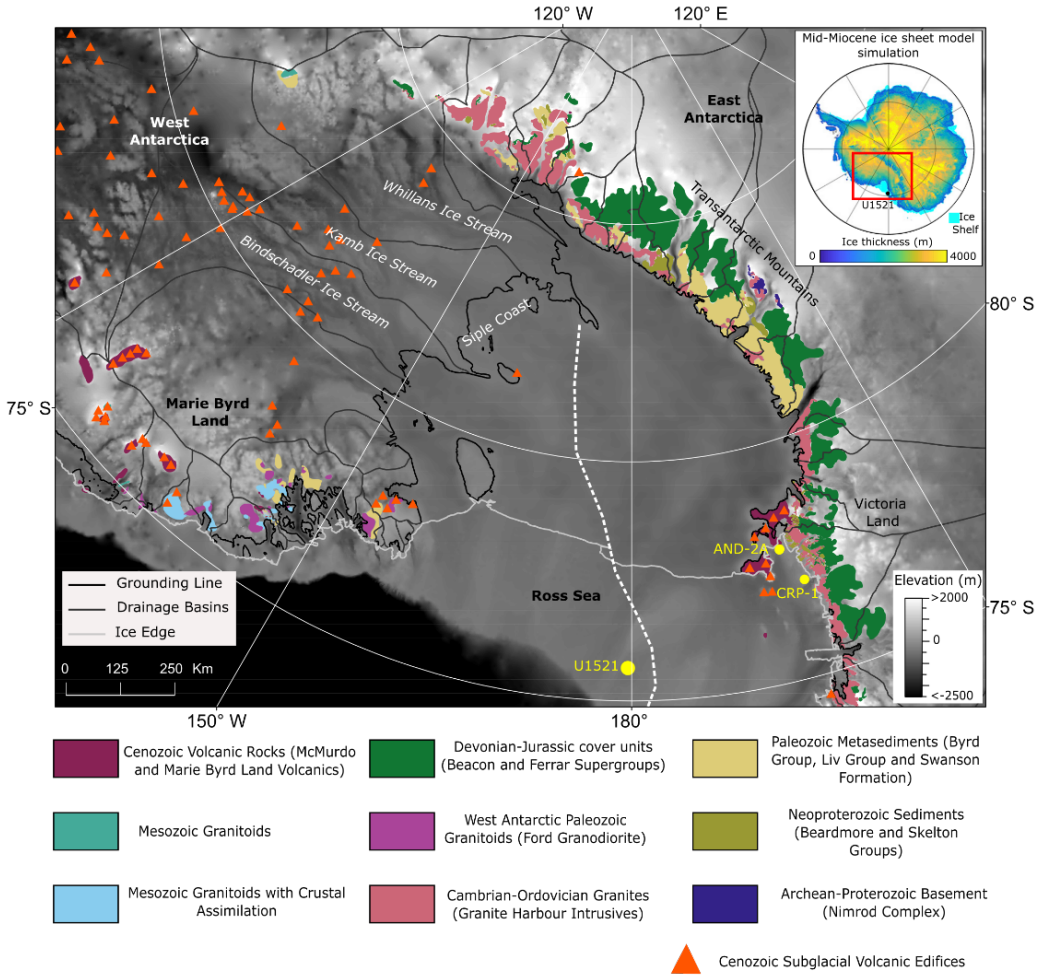
120° W
120° E
West Antarctica
East Antarctica
Whillans Ice Stream
Kamb Ice Stream
Bindschadler Ice Stream
Siple Coast
Transantarctic Mountains
Marie Byrd Land
Victoria Land
Ross Sea
AND-2A
CRP-1
U1521
80° S
75° S
150° W
180°
Mid-Miocene ice sheet model simulation
Ice thickness (m)
0
4000
Ice Shelf
Grounding Line
Drainage Basins
Ice Edge
0 125 250 Km
Elevation (m)
>2000
0
<-2500
Cenozoic Volcanic Rocks (McMurdo and Marie Byrd Land Volcanics)
Devonian-Jurassic cover units (Beacon and Ferrar Supergroups)
Paleozoic Metasediments (Byrd Group, Liv Group and Swanson Formation)
Mesozoic Granitoids
West Antarctic Paleozoic Granitoids (Ford Granodiorite)
Neoproterozoic Sediments (Beardmore and Skelton Groups)
Mesozoic Granitoids with Crustal Assimilation
Cambrian-Ordovician Granites (Granite Harbour Intrusives)
Archean-Proterozoic Basement (Nimrod Complex)
Cenozoic Subglacial Volcanic Edifices

1280

1281

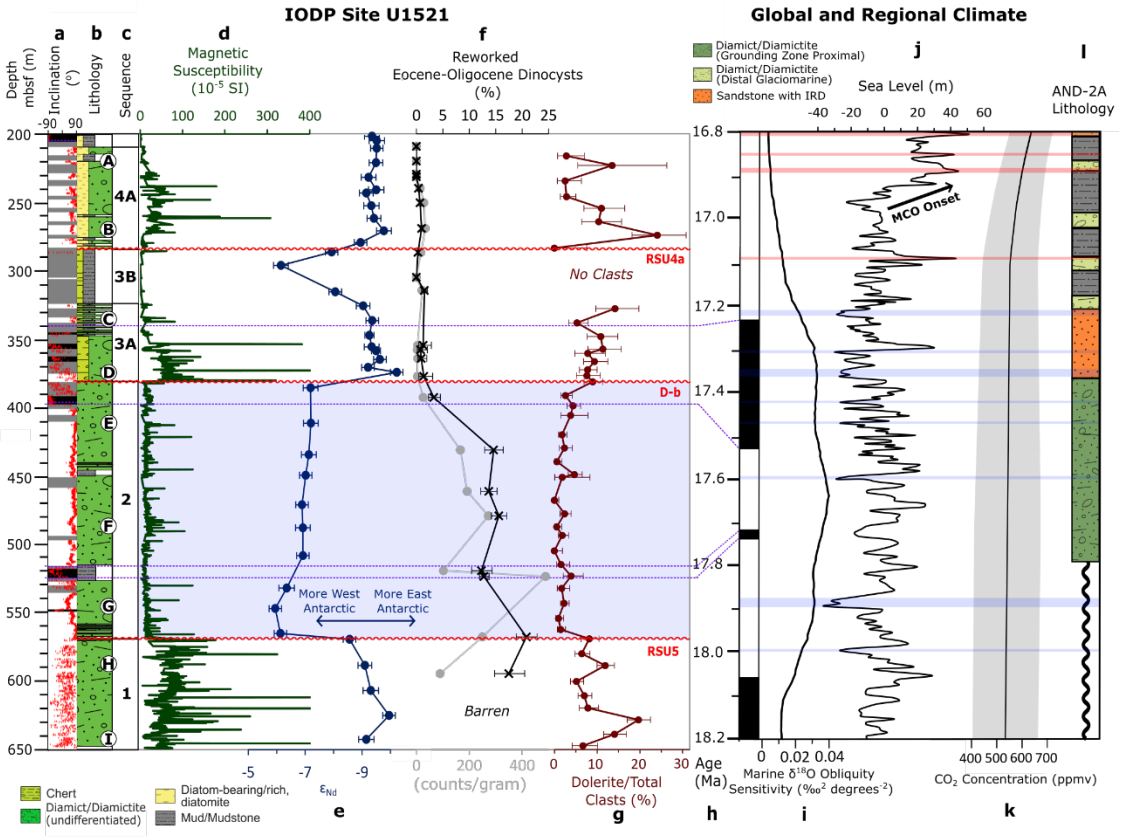
IODP Site U1521
Global and Regional Climate
a
b
c
d
e
f
g
h
i
j
k
l
Depth mbsf (m)
Inclination (°)
Lithology
Sequence
Magnetic Susceptibility (10⁻⁵ SI)
Reworked Eocene-Oligocene Dinocysts (%)
Diamict/Diamictite (Grounding Zone Proximal)
Diamict/Diamictite (Distal Glaciomarine)
Sandstone with IRD
Sea Level (m)
AND-2A Lithology
MCO Onset
RSU4a
RSU5
D-b
No Clasts
Barren
More West Antarctic
More East Antarctic
Chert
Diamict/Diamictite (undifferentiated)
Diatom-bearing/rich, diatomite
Mud/Mudstone
εNd
(counts/gram)
Dolerite/Total Clasts (%)
Age (Ma)
Marine δ18O Obliquity Sensitivity (‰² degrees⁻²)
CO2 Concentration (ppmv)

1282

1283

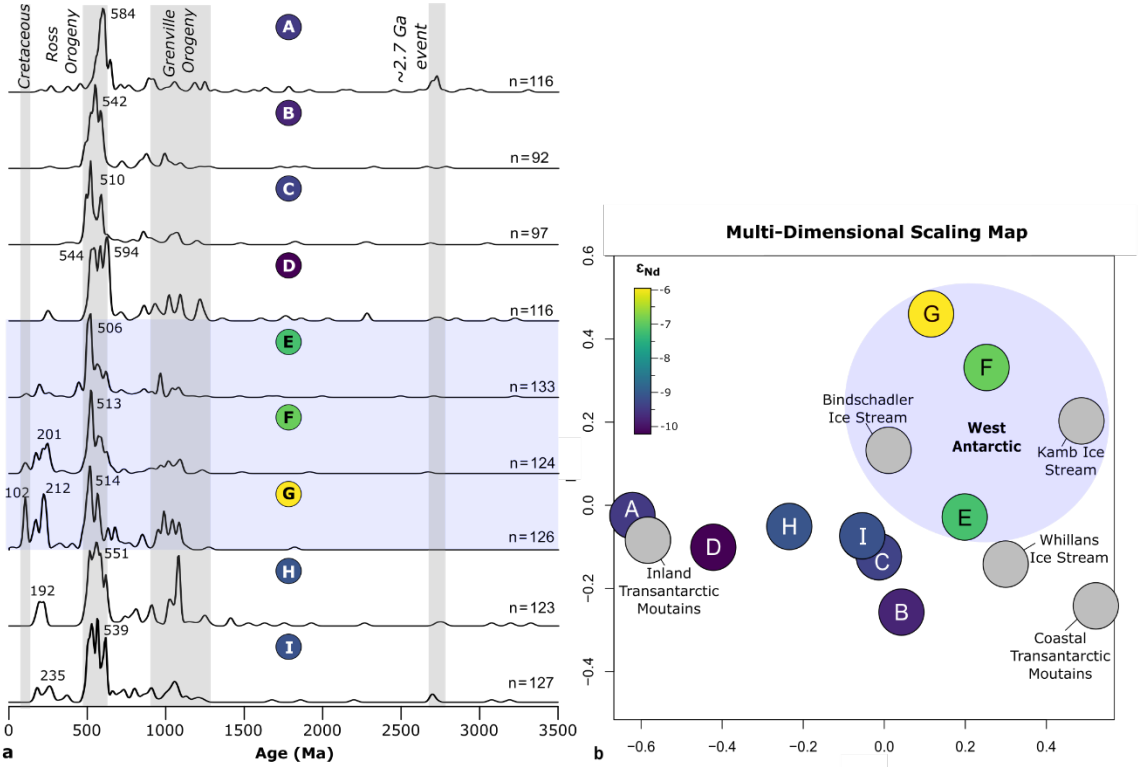
Cretaceous
Ross Orogeny
Grenville Orogeny
~2.7 Ga event
584
542
510
544
594
506
513
201
102
212
514
551
192
539
235
A
B
C
D
E
F
G
H
I
n=116
n=92
n=97
n=116
n=133
n=124
n=126
n=123
n=127
0
500
1000
1500
2000
2500
3000
3500
Age (Ma)
a
Multi-Dimensional Scaling Map
εNd
-6
-7
-8
-9
-10
Bindschadler Ice Stream
West Antarctic
Kamb Ice Stream
Whillans Ice Stream
Inland Transantarctic Moutains
Coastal Transantarctic Moutains
0.6
0.4
0.2
0.0
−0.2
−0.4
−0.6
−0.4
−0.2
0.0
0.2
0.4
b

1284